Surface and Trapping Energies as Predictors for the Photocatalytic Degradation of Aromatic Organic Pollutants

Szymon Dudziak[⸸,*], *Marta Kowalkińska*[⸸], *Jakub Karczewski*[§], *Marcin Pisarek*[‡], *José D. Gouveia*[†], *José R. B. Gomes*[†] *and Anna Zielińska-Jurek*[⸸].

[⸸]Department of Process Engineering and Chemical Technology, Gdansk University of Technology, G. Narutowicza Street 11/12, 80-233, Gdansk, Poland,

[§]Institute of Nanotechnology and Materials Engineering, Gdansk University of Technology, G. Narutowicza Street 11/12, 80-233, Gdansk, Poland

[‡]Institute of Physical Chemistry, Polish Academy of Sciences, Kasprzaka Street 44/52, 01-224, Warsaw, Poland

[†]CICECO-Aveiro Institute of Materials, Department of Chemistry, University of Aveiro, Campus Universitário de Santiago, 3810-193 Aveiro, Portugal

*Correspondence: dudziakszy@gmail.com

Keywords: TiO_2, photocatalysis, crystal facets, regression, prediction.

ABSTRACT

In this study, anatase samples enclosed by the majority of three different crystal facets {0 0 1}, {1 0 0} and {1 0 1} were successfully synthesized. These materials were further studied towards photocatalytic degradation of phenol and toluene as the model organic pollutants in the water and gas phases. Obtained results were analyzed concerning their surface structure, reaction type, and surface development. Moreover, the regression model was created to find the correlation between the possible predictors and photodegradation rate constants (k). From the studied factors, the trapping energy of charge carriers at the surface was found to be the most significant one, exponentially affecting the observed k. This resulted in the overall per-surface activity between the samples being {1 0 1} > {1 0 0} > {0 0 1}. Further introduction of the surface energy (E_{surf}) to the regression model and the number of possible trapping centers per number of pollutant's molecules ($n_{trap}\cdot n^{-1}$) improved the model accuracy, simultaneously showing the dependence on the reaction type. In the case of phenol photocatalytic degradation, the best accuracy was observed for the model including $E_{surf} \cdot (n_{trap}\cdot n^{-1})^{1/2}$ relation, while for the toluene degradation it included E_{surf}^{2} and the $S\cdot n^{-1}$ ratio, where S is simple surface area. Concerning different surface features which influence photocatalytic performance and are commonly discussed in the literature, results presented in this study suggest that trapping is of particular importance.

1. INTRODUCTION

Following early work on the photo-induced reactions over semiconductor particles[1–4], photocatalytic processes has been widely developed and proposed as a possible way to induce redox reactions inside the chemical systems[5–7]. Primarily, environmental and energy-related applications are extensively studied, including photocatalytic water splitting[8,9], H_2 generation[10,11], CO_2 and heavy metal reduction[12–14], as well as degradation of organic pollutants from water and air streams[15–18]. Each of these processes is initiated by the photon absorption and creation of the electron-hole pairs, which can further undergo charge transfer to the substrate present at the surface, inducing its chemical transformation. The efficiency of such transfer and the number of transferred charge carriers directly determine final efficiency of the process and strictly depend on the nature of the photocatalyst. Because of this, many studies focus on designing new photocatalytic materials, which could provide the highest efficiency of such photo-to-chemical energy conversion[19–22], therefore increasing their applicational potential. For an unmodified material, several factors are well-known to be crucial in relation to photocatalytic performance in a specific reactions, such as valence band/conduction band potentials, bandgap type, and light absorption efficiency[23–27]. Due to the suitable band edge alignment, TiO_2 is the most studied photocatalytic material and became almost a standard in photocatalytic degradation processes of different organic pollutants[28–33]. However, significant differences in performance are observed depending on the synthesis conditions, which influence the structural and textural properties of photocatalytic material[34–37]. This suggests that comprehensive studies are still needed to describe what makes specific material an exceptional photocatalyst.

Since the desired charge transfer must occur strictly on the surface, one of the more recent approaches in this aspect is to develop photocatalytic materials with a strictly defined surface structure[38–42]. So far, presented results have shown that the efficiency of the process strongly depends on the nature of the crystal facet exposed at the photocatalyst's surface. However, the exact details on what surface features affect observed performance remain an open question. Different properties, including (i) high surface energy[43,44], (ii) high number of the active sites[45], (iii) efficient trapping and consumption of the charge carriers[39], as well as (iv) efficient adsorption of the substrates[46] being some of the commonly highlighted reasons behind the high photocatalytic activity of such materials. However, majority of the studies presented in the literature considered above parameters separately, without attempts to indicate the dominant factor, which influence mostly on the photocatalytic performance. Simultaneously, from the strictly material design-oriented point of view, it could be desired to know which surface feature could be dominant for the considered reaction. Such approach could help to further design, simulate and optimize photocatalyst surface without extensive experimental work. However, such link between possible surface-related factors and observed activity is hardly found so far.

In this regard, the present study aimed to explain how the surface structure of the anatase affects the photodegradation efficiency of the aromatic organic compounds. Specifically, three questions were raised before this work:

1. Is there a surface structure-related factor that could be identified as dominant one regarding the photocatalytic degradation of organic pollutants?
2. How this dominant factor affects the observed reaction rate (linearly, exponentially or other)?;
3. If the dominant factor can be recognized, what is the impact of the other factors? For example, can they be neglected?

To find answers for these questions, anatase nanoparticles exposing the majority of the {0 0 1}, {1 0 0} and {1 0 1} crystal facets were prepared and used for phenol and toluene photocatalytic degradation in the water and gas phase. Experimental results of degradation were further correlated with well-known factors that describe differences between the exposed facets, such as a surface energy, number of trapping centers and trapping energy. The present work focuses primarily on the simple predictors that should be possible to obtain through computational studies, as it might be helpful for further design of new photocatalytic materials without extensive experimental work.

2. METHODS

2.1. Chemicals

Commercial titanium(IV) oxide P25 (Evonik, Germany), ≥ 96% sodium and potassium hydroxides (POCH, Poland), ≥ 99% titanium *tert*-butoxide (Alfa Aesar, Germany), 50% hydrofluoric acid (w/w, Chempur, Poland), ≥ 99% *n*-butanol (Alfa Aesar, Germany), ≥ 99% ammonium chloride (Sigma Aldrich, Germany) and 25% ammonia solution (w/w, POCH, Poland) were used during the syntheses as received from the manufacturers. Phenol, *ortho*-hydroxyphenol, *para*-hydroxyphenol, *para*-benzoquinone (≥ 98%, Merck, Germany) and toluene (> 99.5%, POCH, Poland) were used as model pollutants/byproducts and standards for calibration. HPLC grade acetonitrile and H_3PO_4 solution (85% w/w) were used for the mobile phase preparation, provided from Merck, Germany. During the gas phase experiments, toluene was dispersed in the synthetic air (Air Liquid, Poland).

2.2. Preparation of the photocatalysts

Anatase TiO_2 nanoparticles, exposing majority of {0 0 1}, {1 0 0} and {1 0 1} facets were synthesized in the three different reaction systems, based on the previous reports[42,47,48]. All reactions were prepared under hydrothermal/solvothermal conditions using Teflon-lined reactors of given volume and the laboratory oven. Presented times include approx. 1-1.5 h of oven heating to the final temperature. Preparation of the {0 0 1} exposed photocatalysts was conducted starting from the 17 cm^3 of titanium tert-butoxide as the Ti source, which was mixed with the 30 cm^3 of *n*-butanol and 3.4 cm^3 of 50% HF solution inside the 200 cm^3 reactor. The prepared mixture was heated up to 210°C for 18 h. Synthesis of the nanoparticles enclosed with the {1 0 0} facets was started by treating 1 g of commercial P25 titanium dioxide with 40 cm^3 of 10 M sodium hydroxide solution inside the 100 cm^3 reactor at the 120°C for 20 h. Obtained Na-titanate product was centrifuged and washed with water until the pH reached a level between 10-11, and half of the product was immediately placed inside the 200 cm^3 reactor without drying. The second synthesis step was carried out using 120 cm^3 of water, and the mixture was heated up to 210°C for 16 h. Finally, preparation of the nanoparticles exposing {1 0 1} facets was conducted similar to the {1 0 0} ones, using 40 cm^3 of 8.5 M potassium hydroxide solution in the first step and heating it to 200°C for 16 h. Obtained analogical K-titanate product was washed with water until pH was between 7-8 and was dried at 80°C. The dried product was grounded, and 0.4 g of the final powder was taken for the second reaction using 100 cm^3 of NH_4Cl/NH_4OH buffer, with the concentration of both compounds being 0.3 M (the pH was around 9). The final reaction was conducted at 210°C for 16 h. All final products were centrifuged and washed with water five times, then dried at 80°C and grounded before further characterization.

2.3. Characterization of the photocatalysts

Obtained materials were analyzed using powder X-ray diffraction (XRD). Measurements were performed using Rigaku MiniFlex diffractometer with Cuα radiation source within the 2θ range between 2-90°. The scanning speed and step were 1 $°\cdot min^{-1}$ and 0.005°, respectively. Morphology of the obtained photocatalysts was observed under the FEI Quanta FEG 250 scanning electron microscope (SEM) after the covering with the Au layer to help remove introduced excess electrons. Based on the observed morphology, the nature of the exposed facets was confirmed by comparing the symmetry of the nanoparticles with the characteristic shapes. Diffuse reflectance spectroscopy measurements in the UV and visible light range (DR-UV/Vis) were performed using Thermo Fisher's Evolution 220 spectrophotometer. Absorption spectra were recorded using $BaSO_4$ as a standard in the incident light's range of 200-800 nm. X-ray photoelectron spectroscopic (XPS) measurements were performed using the PHI 5000 VersaProbe (ULVAC-PHI) spectrometer with monochromatic Al Kα radiation (hν = 1486.6 eV) from an X-ray source operating at 100 μm spot size, 25 W and 15 kV. The high-resolution (HR) XPS spectra were collected with the hemispherical analyzer at the pass energy of 117.4 and the energy step size of 0.1 eV. The X-ray beam was incident at the sample surface at the angle of 45° with respect to the surface normal, and the analyzer axis was located at 45° with respect to the surface. The CasaXPS software was used to evaluate the XPS data. Deconvolution of all HR XPS spectra were performed using a Shirley background and a Gaussian peak shape with 30% Lorentzian character. The obtained powders' surface area was measured using the 10-point Brunauer-Emmet-Teller isotherm method within the p/p_0 range of 0.05-0.3. Analyses were performed with the Micromeritics Gemini V apparatus at the temperature of 77K, using N_2 as the adsorbate. Before the measurements, each sample was degassed at 140°C for 3 h under the N_2 flow

2.4. Photocatalytic degradation of phenol

The photocatalysts' activity was tested toward removing phenol from the aqueous phase as the model reaction for the water purification process. Each sample was analyzed using a 25 cm^3 quartz reactor. Phenol solution was prepared from the stock solution (~500 $mg \cdot dm^{-3}$), and the first sample was analyzed using HPLC/DAD after the dilution and before introducing photocatalysts to check the actual concentration at the start of the process. The prepared suspension of the photocatalyst ((25 ± 0.5) mg in 25 cm^3 of phenol solution) was mixed under a magnetic stirrer with 600 rpm, thermostated to (20 ± 1)°C, and bubbled with (4 ± 0.5) $dm^3 \cdot h^{-1}$ of airflow. The whole system was left for 30 min to achieve adsorption-desorption equilibrium and was further irradiated with the 300 W Xe lamp equipped with the water filter to cut-off infrared light. Prior to the process, the reactor-lamp distance was set up to achieve (30 ± 1) $mW \cdot cm^{-2}$ of the UV flux at the reactor border.

Collected samples were analyzed using Shimadzu Prominence high-pressure liquid chromatography system, combined with the diode-array detector. Separation was performed using Phenomenex C18 column operating at 45°C and with a mobile phase consisting of (v/v) 0.7

acetonitrile, 0.295 water, and 0.05 H_3PO_4 solution (85% w/w). Analyses were performed after the external calibration with pure compounds.

2.5. Photocatalytic degradation of toluene

To study the efficiency of toluene degradation in the gas phase, approximately 0.1 g of each sample was dispersed in 5 cm^3 of water overnight, using a magnetic stirrer, and the prepared suspension was later drop-casted onto the clean glass substrate with the measured dimension to prepared photocatalyst's layer. After applying the suspension, the substrate was dried at 90°C. For each sample, three substrate sizes were used to achieve a different surface area of the photocatalyst. The further degradation process was performed in a flat stainless steel reactor with a working volume of 30 cm^3. The reactor was equipped with a quartz window, two valves, and a septum, with 25 light-emitting diodes (LEDs) acting as the UV light source (λ_{max} = 375 nm). The intensity of the incident UV light above the photocatalyst's layer was (5 ± 0.5) $mW \cdot cm^{-2}$.

In a typical experiment, the prepared substrate was placed in the center of the reactor, and the reactor was filled with the mixture of toluene and synthetic air at a flow rate of 0.17 $m^3 \cdot h^{-1}$ for 1 min (toluene concentration approx. 40 $mg \cdot dm^{-3}$). After this time, the flow was stopped, and the reactor was closed with the valves. Before the photocatalytic process, the system was kept in the dark for 40 minutes to achieve an adsorption-desorption equilibrium, followed by 30 minutes of LED irradiation. The concentration of toluene was measured chromatographically by collecting gas samples from the reactor through the septum using a gastight syringe. Analysis was performed using a gas chromatograph (Clarus 500, PerkinElmer) equipped with a flame ionization detector (FID) and DB-1 capillary column (30 m × 0.32 mm, film thickness 3.0 μm). Prior to the analysis, calibration was performed using toluene samples with known concentration.

2.6. Analysis of the results concerning surface energy and trapping energy

Obtained degradation results were analyzed with respect to the reported values of surface energy, as well as trapping energy of e^- and h^+ at the models of the (0 0 1), (1 0 0), and (1 0 1) surfaces[49,50]. The values of both predictors, presented in Table 1, were obtained from the works of Lazzeri *et al*. for the surface energy[49] as well as Ma *et al*. in the case of trapping energies[50]. Prior to the analysis, the results of toluene and phenol degradation were transformed from initial $mg \cdot dm^{-3}$ to the $mmol \cdot dm^{-3}$ and the rate constant k was determined assuming I-order kinetics, as commonly observed during the photocatalytic reactions:

$$k = d\ln(C_0/C) \cdot dt^{-1}$$

where C_0 is pollutant concentration at the start of the irradiation, d is derivative and t is time. For further analysis, the total number of the pollutants' molecules in the reaction system was also calculated to compare with the photocatalyst's surface area[51]. Different phenol concentrations and different sizes of the photocatalyst layer were used to achieve a different amount of phenol/toluene molecules reacting per surface unit of each structure. The photocatalyst concentration was fixed for water phase experiments to minimize its effect on each series' light-scattering inside the slurry[52]. Furthermore, additional analysis was also performed upon considering the total number of undercoordinated species on each surface that could act as the trapping center for both charge carriers. In this case, the total surface area was replaced with the calculated number of "active" atoms.

Obtained experimental data were statistically modelled using regression analysis to find the correlation with all considered predictors. Analysis was started from the simple correlation between available surface area (or the number of active sites) and the number of pollutants' molecules. This arranged all results within the 3 groups, depending on the surface type. The further analysis considered the difference between those groups to be purely surface-type dependent.

Ultimately, different models were analyzed, and their fit to the experimental data was monitored using the residual sum of squares (RSS) to find the best correlation.

Table 1. Reported surface energies and trapping energies of e^- and h^+ on the different anatase surfaces. Presented values correspond to models in vacuum.

Surface model	Surface energy ($J\cdot m^{-2}$)	Trapping energy e^- ($J\cdot 10^{-19}$)	Trapping energy h^+ ($J\cdot 10^{-19}$)	Refs.
(0 0 1)	0.90	0[a]	0.77	49,50
(1 0 0)	0.53	0.83	1.47	
(1 0 1)	0.44	2.13	1.67	

[a] Reported trapping do not occur at the surface atoms

2.7. Electron localization on an F-modified anatase TiO_2 (0 0 1) surface

To study possible electron trapping on the fluorinated {0 0 1} anatase facet additional density functional theory calculations (DFT) of the (0 0 1) surface slab model were performed using the VASP code. The DFT calculations considered dipole-corrections, spin polarization, and the Perdew-Burke-Ernzerhof (PBE) exchange-correlation functional, including D3 dispersion corrections to correctly describe the van der Waals interactions. The wave function of valence electrons was expanded using a plane-wave basis set with an energy cut-off of 415 eV, with core electrons implicitly considered with the projector augmented-wave (PAW) method. Orbital occupations were set using Gaussian smearing with a width of 0.01. Convergence criteria for total energies and for atomic positions were 10^{-5} eV and 0.01 eV/Å, respectively. The Brillouin zone was sampled with a 4×4×1 Monkhorst-Pack grid of special k-points.

The prepared model consisted of the (0 0 1) surface of TiO_2 as a 3×3 periodically repeated slab with 18 TiO_2 layers (6 Ti layers), terminated by O on one side (the “bulk” side of the slab) and by F on the other side (the “free” side of the slab). During atomic position optimizations, the 9 bottom

Commented [JRBG1]: Please add here the following four references:

G. Kresse, J. Hafner, Ab initio molecular dynamics for liquid metals, Physical Review B. 47 (1993) 558–561. https://doi.org/10.1103/PhysRevB.47.558.

G. Kresse, J. Hafner, Ab initio molecular-dynamics simulation of the liquid-metal–amorphous-semiconductor transition in germanium, Physical Review B. 49 (1994) 14251–14269. https://doi.org/10.1103/PhysRevB.49.14251.

G. Kresse, J. Furthmüller, Efficient iterative schemes for ab initio total-energy calculations using a plane-wave basis set, Physical Review B. 54 (1996) 11169–11186. https://doi.org/10.1103/PhysRevB.54.11169.

G. Kresse, J. Furthmüller, Efficiency of ab-initio total energy calculations for metals and semiconductors using a plane-wave basis set, Computational Materials Science. 6 (1996) 15–50. https://doi.org/10.1016/0927-0256(96)00008-0.

Commented [JRBG2]: Please add this reference after PBE,

J.P. Perdew, K. Burke, M. Ernzerhof, Generalized Gradient Approximation Made Simple, Physical Review Letters. 77 (1996) 3865–3868. https://doi.org/10.1103/PhysRevLett.77.3865.

Commented [JRBG3]: Please add after corrections the following references:

S. Grimme, J. Antony, S. Ehrlich, H. Krieg, A consistent and accurate ab initio parametrization of density functional dispersion correction (DFT-D) for the 94 elements H-Pu, The Journal of Chemical Physics. 132 (2010) 154104. https://doi.org/10.1063/1.3382344.

S. Grimme, S. Ehrlich, L. Goerigk, Effect of the damping function in dispersion corrected density functional theory, Journal of Computational Chemistry. 32 (2011) 1456–1465. https://doi.org/10.1002/jcc.21759.

Commented [JRBG4]: Please add here the following ref.

P.E. Blöchl, Projector augmented-wave method, Physical Review B. 50 (1994) 17953–17979. https://doi.org/10.1103/PhysRevB.50.17953.

Commented [JRBG5]: Please add here the following ref.

H.J. Monkhorst, J.D. Pack, Special points for Brillouin-zone integrations, Physical Review B. 13 (1976) 5188–5192. https://doi.org/10.1103/PhysRevB.13.5188.

most TiO_2 units and the oxygen termination were fixed to mimic the bulk structure[53]. The width of the slab was approx. 16 Å and the simulation box height was fixed at 28 Å, leaving 12 Å of vacuum width to avoid interaction between periodic replicas of the system in the direction perpendicular to the surface.

In order to force charge localization on the surface Ti site two steps were performed[54–56]. Firstly, the wavefunction of the selected Ti was changed to V, creating a singly negatively charged TiO_2 system since neutral V atom contains one more electron than a neutral Ti. Also, the V atom contains one more proton in its nucleus than a Ti one, it attracts electrons more strongly. The second step for localizing charge around a Ti atom consists of replacing the V atom with a Ti one again, and using the wavefunction obtained in the first step as starting point for calculating the electronic density of the TiO_2 system.

3. RESULTS & DISCUSSION

3.1. Photocatalysts' characterization

The crystal structure and morphology of the prepared photocatalysts were analyzed with powder XRD measurements and SEM observations to confirm their desired structure. The obtained XRD patterns and selected images from the electron microscope are presented in Figures 1 and 2, respectively. The single-phase anatase structure was present for all samples, only with some differences in the relative intensity of selected signals. This is in agreement with the expected shape variance between the samples since both different sizes of the crystal in a specific direction, and their orientation to the X-ray source should affect the width and intensity of the reflections[40]. In this regard, especially broadening of the (0 0 4) and (1 0 5) signals for the {0 0 1} sample is in agreement with the expected size reduction along with the [0 0 1] direction, which by now is a well-documented effect[57–63]. Furthermore, similar features might also be noticed for the {1 0 0} sample, specifically a broadening of the (2 0 0) signal and the sharp (0 0 4) one. Moreover, for the {1 0 1} sample, no significant broadening of any reflections was noted, with a characteristic higher intensity of the (1 0 5) reflection, compared to the (2 1 1), around 55° [64,65].

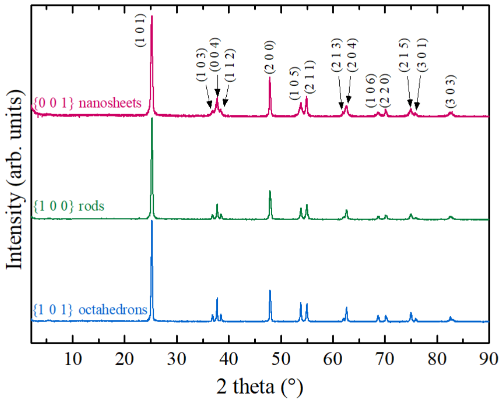

Figure 1. XRD patterns of the obtained samples. All reflections correspond to the anatase TiO_2 crystal structure.

Furthermore, based on the observed width of the XRD reflections, the approximate size of the crystallites in different crystallographic directions was calculated, as shown in Table 2. As observed, the relative difference in the observed dimensions match quite well the expected trends. Especially, crystallites size along with the [0 0 1] direction, calculated from the (0 0 4) reflection, is the lowest for the sample exposing {0 0 1} and the highest for the {1 0 0} one. Moreover, the sample exposing {0 0 1} is the only one with the higher size observed along the [1 0 0] direction, based on the (2 0 0) reflection, than [0 0 1].

Table 2. Calculated crystallites size in different crystallographic directions.

Sample	Crystallites size (0 0 4) (nm)	Crystallites size (2 0 0) (nm)	Crystallites size (1 0 1) (nm)
{0 0 1}	22	38	39
{1 0 0}	149	115	46
{1 0 1}	81	46	41

Nevertheless, since XRD analysis alone is not sufficient for the determination of exposed facets, it was further completed with the morphology observation for all samples. The expected shape of the nanocrystal in each case can be obtained based on the Wulff theorem and the known symmetry of anatase structure[66]. The comparison between expected and observed morphologies are presented in Figure 2. As shown, the real samples match their theoretical constructs very well, with rectangular sheets, rectangular rods, and octahedrons being formed for the samples exposing the {0 0 1}, {1 0 0} and {1 0 1} facets, respectively. The formation of each structure results directly from the combination of HF with *n*-butanol in case of the {0 0 1} sample[67,68], as well as from the pH increase during the growth of the {1 0 1} structures (pH ~ 9) and the {1 0 0} ones (pH > 10)[69].

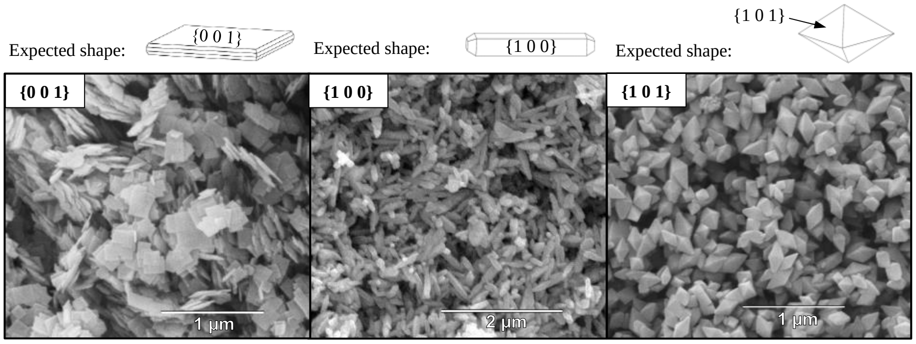

Figure 2. SEM images of the obtained samples and their expected shapes, based on the designed facet exposition.

Furthermore, to study the possible defects' formation inside the obtained nanoparticles additional DR-UV/Vis and XPS studies were performed. As shown in Figure 3, all of the samples possess similar surface composition, with Ti 2p and O 1s signals being typical for the stoichiometric TiO_2. Especially, no signs of Ti^{3+} states are visible for all samples as well as the amount of non-lattice oxygen is both limited and similar between different structures. These additional O signals could be easily connected with the presence of adsorbed carbon species on the samples' surface, which is typical during the XPS analysis. The only noteworthy feature is clearly visible presence of fluoride on the surface of sample exposing {0 0 1} facets, which match reported signals for the fluorinated TiO_2 (approx. 684.5 eV). Fluorine presence resulted from the HF introduction during the synthesis and is typical for the HF-mediated stabilization of the {0 0 1} facets. No signs of a lattice O substitution by F is observed (XPS signals for the binding energy ≥ 685 eV[70–72]), therefore all of the observed fluoride is simply adsorbed on the surface Ti. The atomic F/Ti ratio is 0.25.

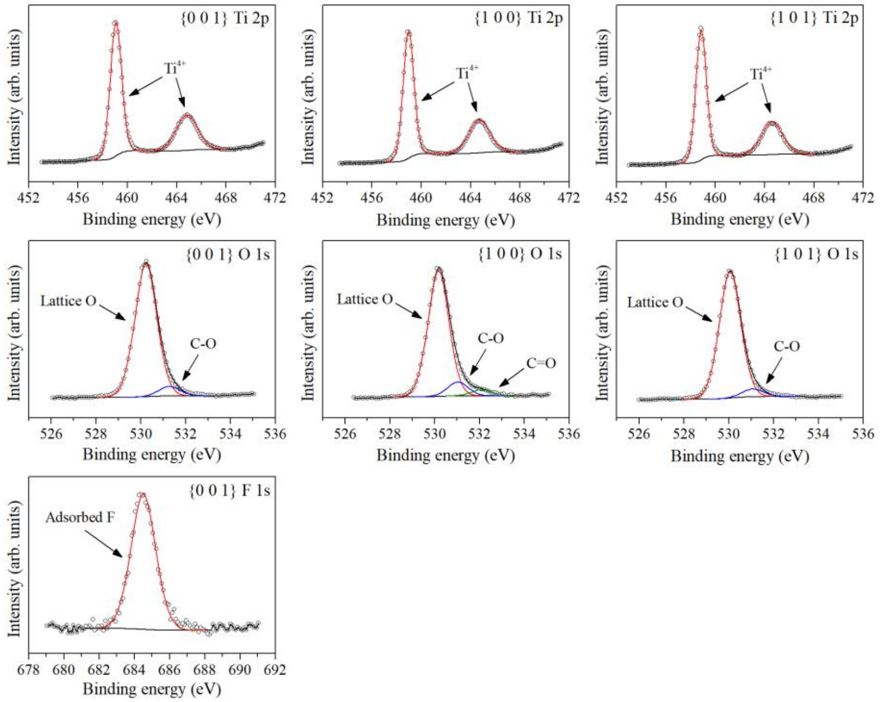

Figure 3. XPS signals observed for the Ti, O and F states on the surface of each nanostructure.

Moreover, as shown in Figure 4, the energy of the valence band edge observed during the XPS studies is very consistent between the samples, showing that no shifts in the Fermi energy level is present. Especially, this shows that no acceptor defect states should be present above the valence band edge for each nanostructure.

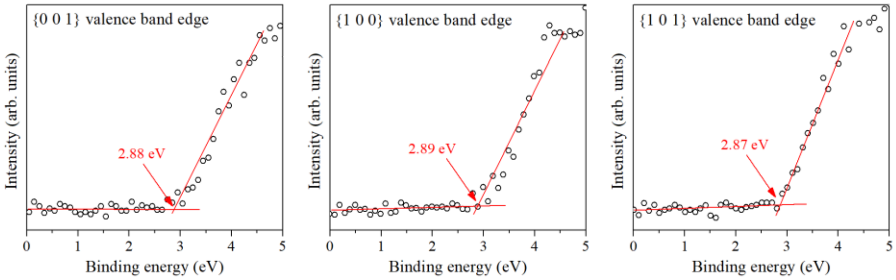

Figure 4. Valence band edge observed for each sample during the XPS studies.

Finally, the absorption spectra of the prepared samples are shown in Figure 5a. Similarly to the XPS studies, no significant difference in the observed signals is noticed and especially no defined peaks are present for λ > 400 nm. Furthermore, the absorption edge for the valence-to-conduction band excitation is almost the same for all nanostructures and the corresponding bandgap values are very similar for all samples (Figure 5b). Comparing this with the position of the valence band edge from Figure 4, it can be seen that the Fermi level of all samples is also similar and lies approx. 0.35 eV below the conduction band edge. This is reasonable with the anatase being n-type semiconductor and further proves that no significant concentration of defects should be present within each sample, as well as they do not alternate the surface states of the photocatalyst, as evidenced by the XPS. In this regard the surface structure of all samples is expected to closely represent their theoretical models, excluding F adsorbed on the {0 0 1} facets, which justify analysis of their activity with respect to the different predictors presented in the computational studies.

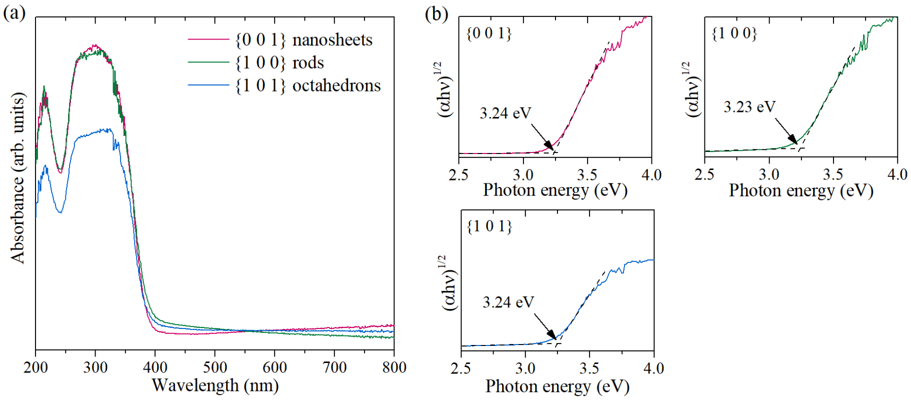

Figure 5. DR-UV/Vis absorption spectra of the obtained TiO_2 samples, exposing different crystal facets (a), as well the corresponding Tauc's plots and determined bandgap values (b).

3.2. Photocatalytic degradation in water and gas phase

Prior to testing the photocatalytic activity of the obtained materials, the surface area of the powders was measured using the BET method, and the masses of the photocatalyst's layer on the substrate were precisely determined. These data were summarized in Table 3, together with the exact photocatalysts mass introduced during the water phase experiments and the initial concentration of phenol (to account for possible error during dilution). Regarding the gas phase experiments, the toluene concentration was fixed between the processes. Therefore, it was not considered to affect observed differences between the samples.

Table 3. Summation of the experimental factors affecting observed degradation efficiency, as measured before the photocatalytic tests.

Sample	Aqueous phase	Gas phase

	BET surface area ($m^2 \cdot g^{-1}$)	Photocatalyst mass (mg)	Initial phenol concentration ($mmol \cdot dm^{-3}$)	Photocatalyst's layer mass (mg)
{0 0 1}	38	24.99	0.332	10.02
		25.14	0.217	16.28
		25.41	0.108	32.65
{1 0 0}	13	25.41	0.323	10.59
		24.99	0.207	19.12
		25.05	0.108	28.08
{1 0 1}	13	24.57	0.319	5.74
		24.47	0.203	12.53
		24.59	0.101	14.71

Furthermore, Figure 6 presents the as-observed photocatalytic degradation rates of phenol and toluene over the prepared samples and the slope of the fitted line defines the reaction rate constant *k*. A visible effect of all three factors can be observed from the very start of the analysis (surface type, phenol concentration/layer area, and gaseous/aqueous environment). In each case, increasing the number of pollutant molecules reacting per surface of the photocatalyst lowered the observed rate constant. This is in agreement with the expected outcome since an increase of the surface area is known to promote faster reaction rates, as it provides more active centers for the reaction to occur[51]. Similarly, changing the amount of reacting pollutant will give the same result, and the final reaction rate will increase proportionally to the $S \cdot n^{-1}$ ratio. This ratio should roughly represent the number of active centers that are "free" to react with a single pollutant's molecule (S is total surface area and n is a number of the pollutant's molecules). The same relation was also observed previously for the series of different {0 0 1} exposed anatase nanosheets[42].

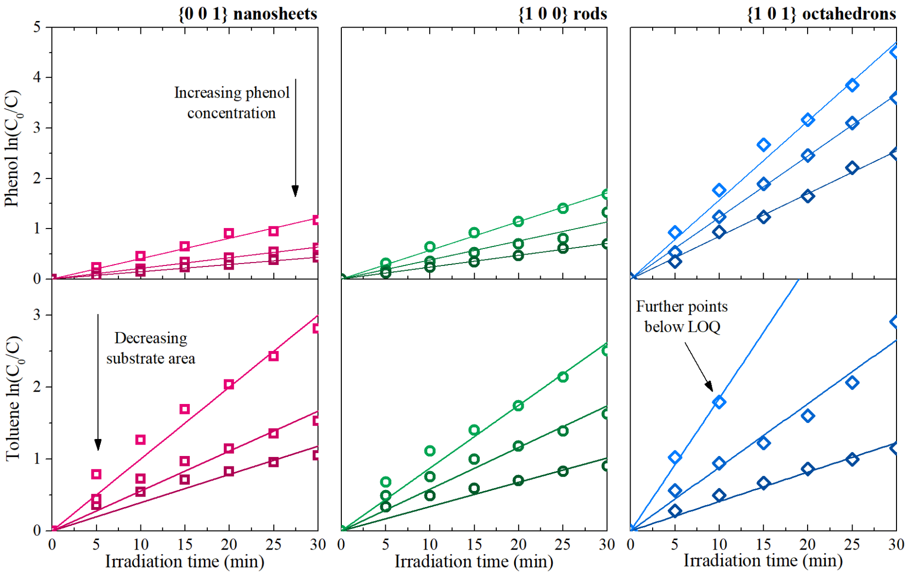

Figure 6. As-obtained phenol and toluene degradation results over the prepared samples, without accounting for possible factors (LOQ stands for "limit of quantification"). The slope of the fitted lines is rate constant (k) for the I-order reaction $ln(C_0/C) = k \cdot t$.

Ultimately, Figure 7 presents detailed results of the phenol degradation and formation of its aromatic-byproducts, including *ortho* and *para*-hydroxylated species. As observed, the amount of degraded phenol strictly correlates with the amount of the oxidized species, proving that observed kinetics of phenol removal represent its chemical transformation, rather than a photo-stimulated adsorption. For the highest removal rates (the {1 0 1} samples) the rapid formation of observed by-products is followed by their further disappearance, which is expected in case of a step-by-step oxidation. For all series, increasing initial phenol concentration results in the higher amounts of formed by-products and their slower subsequent removal. This would fit the expected results as the number of "free" active sites should be lower when the amount of initial pollutant increase, therefore, further reaction of by-products became limited and their higher accumulation is observed.

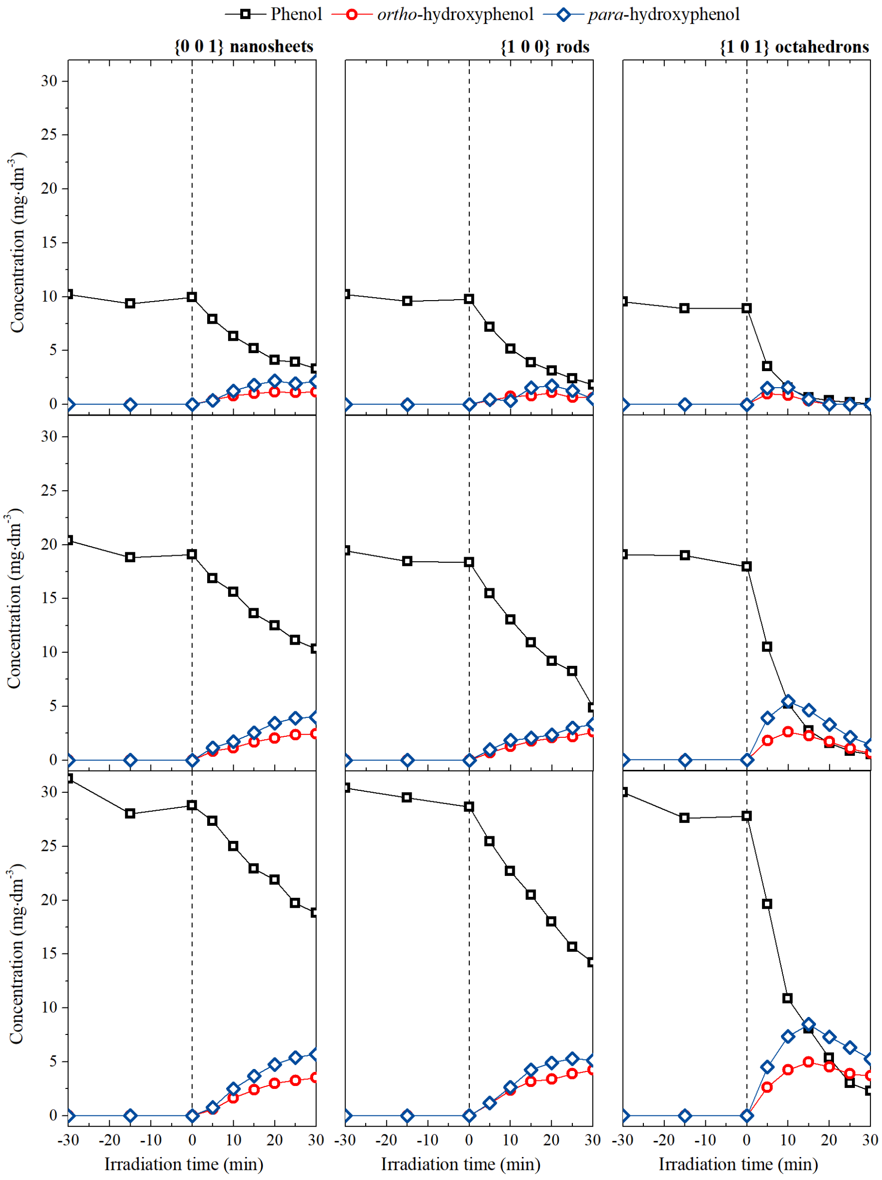

Figure 7. Detailed results of the photocatalytic phenol degradation in the aqueous phase.

Regarding the surface structure, the high activity of the {1 0 1} enclosed octahedrons was noticed for both reactions, while it especially dominated in the aqueous phase. This is despite the lowest surface area of this sample. Therefore, the surface energy should not be a dominant factor for both reactions since the {1 0 1} surfaces possess the lowest surface energy. In the aqueous phase, all samples clearly followed the per-surface activity order of {1 0 1} > {1 0 0} > {0 0 1}, which is in agreement with some other studies that have shown relatively low activity of the {0 0 1} surfaces[38,39]. On the other hand, the difference between the octahedrons and other structures is less visible in the gas phase.

Concerning the {0 0 1} nanosheets and {1 0 0} rods, they revealed similar activity in both reactions, however the measured surface area of the {0 0 1} nanosheets was still 3 times larger than that of the {1 0 0} rods. However, the surface area exposed to the reaction system is hard to be accurately provided in the gas phase, due to the unknown porosity of the prepared layer. In such case, the facile measurement of the photocatalyst's layer area may be inaccurate because particle geometry affects the roughness of the layer and further diffusion of the substrate through the film[73]. Therefore, an approach similar to the aqueous phase was applied, assuming the total possible area of the photocatalyst through measured mass and BET results. That should partially correct the effect of the particles' morphology on the actual area available for the reaction in the gas phase. By accepting this approach, the per-surface activity order in the gas phase became the same as in water, due to the high surface area of the {0 0 1} samples. However, these differences are less noticeable than for phenol degradation. Ultimately, this suggests that surface energy might be a more important factor during the gas phase process. These results are shown in Figure 8, in which observed k is presented concerning the $S{\cdot}n^{-1}$ ratio, clearly dividing the data into three series, depending on the surface type. These could be described as:

$$k = a \cdot S \cdot n^{-1}$$

where k is rate constant defined by the slope in Figure 6, a is fitted constant, S is total surface area of the photocatalyst during the process, defined by its mass and BET surface area, and n denotes is the amount of pollutant's molecules at the start of the process. Specifically:

$$n = \frac{C_{mmol} \cdot V \cdot N_A}{1000}$$

where C_{mmol} is pollutant's concentration in mmol·dm^{-3}, V is reactor volume in dm^{3} and N_A is Avogadro's number. Starting from this point, the slope of the fitted lines in Figure 8 (a parameter) should depend strictly on the nature of the exposed facet. Therefore, further analysis of the fitted a was performed with respect to the discussed predictors.

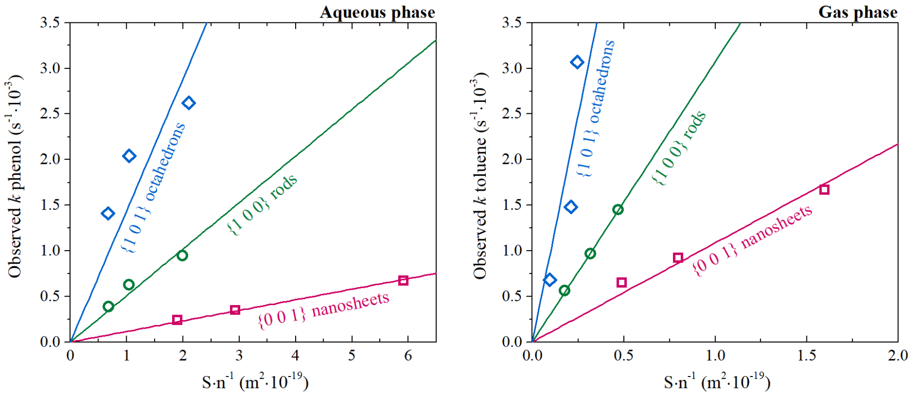

Figure 8. Obtained results of phenol and toluene degradation with respect to the ratio between the total surface area of the photocatalyst (S) and the number of the pollutant's molecules at the start of the process (n).

3.3. Analysis with respect to trapping energy

Since octahedral particles, enclosed with the {1 0 1} facets, was found to be the most photocatalytic active in both reactions, analysis of the fitted a was started by finding its correlation with the trapping energy, which is the highest for this surface (see Table 1). Figure 9 shows *a* as a function of total trapping energy E_{trap} (simple sum of both electron and hole trapping energies), together with an additional (0, 0) point, representing hypothetical situation of no surface present.

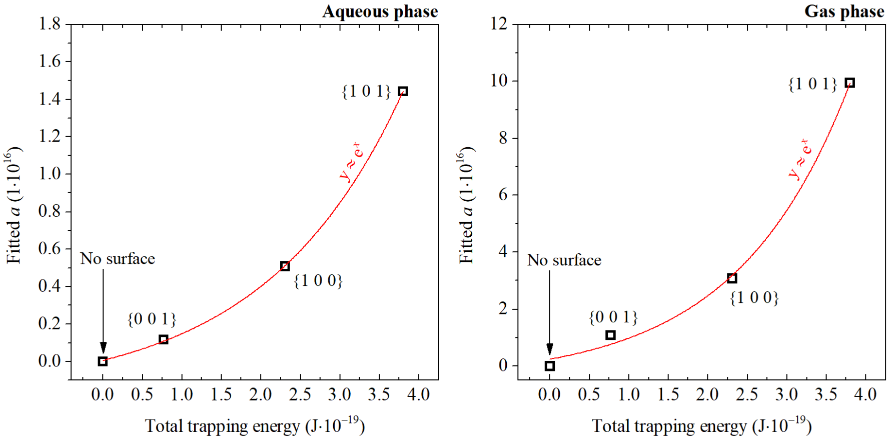

Figure 9. Correlation between observed *a* parameter and the total trapping energy (sum of electron and hole trapping energies) reported for each surface. The presented $y = e^x$ line is drawn here only to highlight the general correlation.

In the case of both reactions, this relation follows the exponential character, which could be specially connected with the possible distribution of the trapped states. As suggested by Ma *et al.*, the difference in the trapping energy should influence the distribution of the trapped states, following Boltzmann distribution[50]. Then, the concentration of these states should affect the actual performance observed during the photocatalytic reaction. Therefore, further analysis was performed, assuming the general formula of:

$$a = b \cdot \left(e^{\frac{c \cdot E_{trap}}{k_B T}} - 1 \right)$$

where a is analyzed slope from Figure 8, E_{trap} is total trapping energy, as defined before, k_B is Boltzmann's constant, T is absolute temperature and b, c are further fitted parameters. The summation of this analysis is presented in Table 4, showing an excellent correlation in both cases. Moreover, it could be further reasoned that obtained c parameter probably indicates the fraction of the trapped charge carriers that effectively react at the surface. During the photocatalytic degradation of aromatic pollutants, the generation of different reactive oxygen species (ROS) is crucial, and the actual oxidation is often initiated by the attack of generated radicals[29,74]. Therefore, step-by-step illustration of the process could be divided into four consecutive processes, namely: (i) generation of charge carriers, (ii) their trapping at the surface, (iii) surface reaction to generate ROS, and (iv) reaction between ROS and the pollutant. Possible reactions (Equations 1-7) are shown below for the photogenerated charge carriers[28,75,76]:

$$TiO_2 + hv \rightarrow h^+ + e^- \qquad (1)$$

$$h^+ \rightarrow h^+_{trapped} \qquad (2)$$

$$e^- \rightarrow e^-_{trapped} \qquad (3)$$

$$h^+_{trapped} + H_2O \rightarrow \cdot OH + H^+ \qquad (4)$$

$$e^-_{trapped} + O_2 \rightarrow \cdot O_2^- \qquad (5)$$

$$\cdot OH + A \rightarrow A\text{-}OH \qquad (6)$$

$$\cdot O_2^- + AH \rightarrow \cdot A + HO_2^- \qquad (7)$$

In this study, the rate constant of the final steps that leads to the chemical transformation of the pollutant (6) and (7) was calculated, while especially the reactions (2) and (3) should be driven by the analyzed trapping energy. However, it seems not possible for all trapped states to effectively contribute to the final rate, since it would imply that reactions (4-7) are occurring with 100% efficiency. Therefore, the c parameter must appear to “slow down” the process rate that could be expected from the simple increase of the trapping energy. Moreover, although the strict interpretation of the c parameter is not obvious, it could be noted that its values of approx. 0.02-0.03 are close to the reported photonic efficiency of ·OH generation by the TiO_2 (approx. 3%[77]). In this regard, it might be suggested that these parameters are somehow connected, *e.g.* both will be affected by the possible surface recombination. Ultimately, it is shown that the observed rate should follow trapping energy exponentially, with the exponent being $E_{trap}/k_BT \cdot c$ and c might be a fraction of maximum possible trapped states that will effectively influence on the reaction.

Table 4. Results of a fitting to the expression $a = b \cdot (e^{Etrap/kBT \cdot c} - 1)$.

$a = b \cdot (e^{Etrap/kBT \cdot c} - 1)$	R^2	Fitted b	Fitted c	Reported photonic efficiency of ·OH generation by TiO_2	Ref.
Aqueous phase	0.9998	$1.93387 \cdot 10^{15}$	0.02275	between 0.029 to 0.035	77
Gas phase	0.9936	$9.66209 \cdot 10^{15}$	0.02581		

At this point, straightforward prediction of k, based on the calculated $S \cdot n^{-1}$ ratio and analyzed trapping energy, reproduces the overall activity order well. This indicates that E_{trap} is probably the most important factor affecting the final rate. Although, it is not possible to directly identify reaction steps through such analysis, these results are in agreement with *e.g.* general mechanism of ·OH formation on the anatase TiO_2 surface presented by Nosaka and Nosaka, which include h^+ trapping on the surface O atom and subsequent H_2O attack[28]. However, Shirai *et al*. reported that details of such process might differ between the spherical and faceted particles. In particular, the water-assisted hole trapping was not observed for the {0 0 1} and {1 0 1} anatase facets and the {1 0 0} was not considered[78]. In this regard the detailed mechanism of possible reaction (4) might not be obvious for all nanostructures and a more complex mechanism might be discussed. First of all, as shown by Chen *et al.*, formation of the ·OH radicals on {1 0 1} facet might involve h^+ trapping on the surface 3-fold coordinated O atom and subsequent transfer to the terminal -OH group, which was found to be an energetically favorable process[79]. This might be further reasoned since -OH groups are commonly observed on the TiO_2 surface *e.g.* on the FTIR spectrum[80]. Furthermore, other species are also expected to be present at the photocatalyst surface, depending on the environment (gas/liquid, pH, O_2 concentration, adsorbed pollutant), which could further affect charge carriers trapping and transfer[81]. As recently reported by Hwang *et al*., formation of ·OH might also include reductive path from O_2, which contributed to approximately 1/3 of the observed oxidation product of benzoic acid over anatase particles[82]. During such reaction, H_2O is expected to react with the surface O_2 in the presence of excited electrons. As reported by Setvin *et al*., this specific process on the {1 0 1} facet induce dissociation of water to OOH^- and OH^-, which becomes almost a barrierless reaction[83]. Therefore, due to the reduction process on the {1 0 1} facet, generation of the ·OH radicals might also be increased through the subsequent oxidation of OH^-, rather than H_2O itself. This might also be stimulated by the relatively high water adsorption and Lewis acidity, previously reported for this surface[80].

Unfortunately, due to the limited number of such detailed studies, similar cooperation between the reduction and oxidation of oxygen/water can be analyzed in detail only for the {1 0 1} facets. Therefore, more detailed studies on the reactivity of all these facets to generate different ROS, *e.g.* in the different environment, are planned to give better insight into the details of their possible formation. Nevertheless, since presented description of the possible reactions on the {1 0 1} combine both h^+ and e^- processes to improve each other (i) e^-/O_2 inducing dissociation of water, which is unfavored in other cases, and (ii) h^+ reacting with the OH^-, generated as a one of the products of this dissociation, it would fit the presented trend nicely, explaining why high trapping energy of both charge carriers on the {1 0 1} facets resulted in its highest observed activity. Ultimately, Figure 10 shows plots of predicted vs observed k for both reactions, when only trapping energy was considered to determine *a*, as well as calculated residuals for both cases (k_{model} - k_{obs}). Specifically:

$$k = b \cdot \frac{S}{n} \cdot \left(e^{c \cdot \frac{E_{trap}}{k_B T}} - 1\right)$$

As seen. especially in the case of phenol degradation, some points are predicted very well. However, the overall error might still achieve quite large values, especially for the high *k* (up to 40% of the observed rate constant), as well as predictions for toluene are generally erroneous, despite the overall trend being preserved. In this regard, other factors that might improve possible predictions were studied.

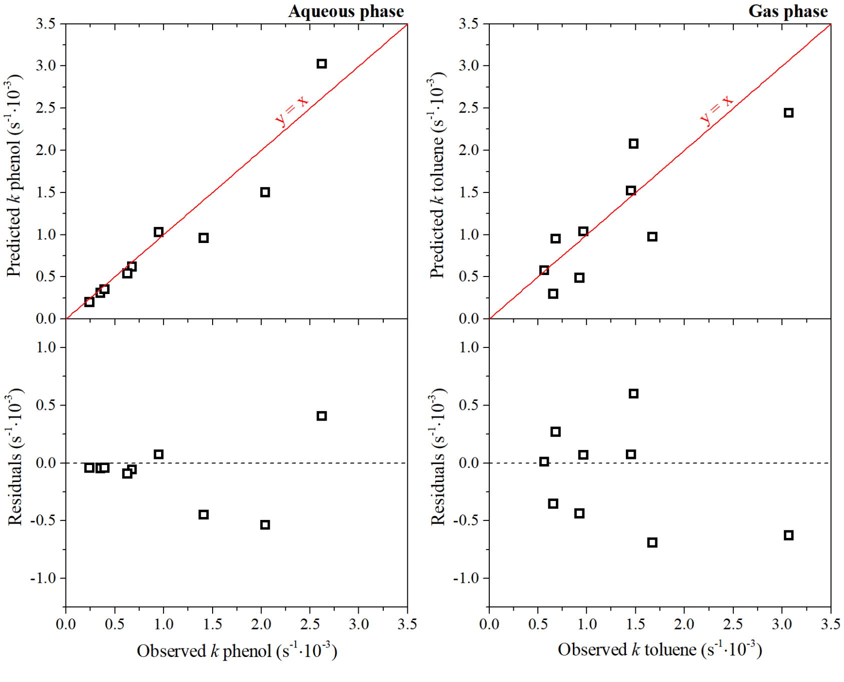

Figure 10. Predicted vs observed *k* and the residual plot for both reactions, obtained with the model considering only trapping energy and the $S \cdot n^{-1}$ ratio. Parameters obtained from the regression analysis are presented in Table 4.

3.4. Further analysis concerning surface energy and the number of trapping centers

The analysis described in the previous section focused on the reported trapping energies of holes and electrons on the obtained anatase crystals surfaces. These energies should especially influence the probability of charge carriers' trapping at the surface, which could react with other substrates, as outlined in the previous section. However, to describe the whole process properly, this should be further connected with the number of trapping centers and the number of reacting molecules at the surface. Initially, it was assumed to be proportional to the $S \cdot n^{-1}$ ratio; however, further considerations might be made to improve this relationship. First of all, it is known that different surfaces have different numbers of different-coordinated atoms that could effectively trap both charge carriers. Although it was highlighted before that specific trapping behavior can change due to the presence of adsorbates, the details are not presented for all surfaces[78,84]. Therefore, at this point we will follow the trapping description presented in the same study as adopted trapping energies (in vacuum), since they are strictly connected and still allow to relatively compare analyzed facets. Based on these results, the theoretical number of surface atoms that could effectively start the reaction was calculated. For the (1 0 0) and (1 0 1) surface models, this is equal to a number of both 5-fold coordinated Ti atoms (5f-Ti) and 2-fold coordinated O atoms (2f-O), as both electrons and holes should effectively localize on them[50]. However, in case of the (1 0 0) surface Ma *et al.* have shown that these electrons partially delocalize over the surface 5f-Ti atoms[50]. In this regard, it could be expected that not all Ti sites can effectively trap e^- for this surface. Therefore, the density of 5f-Ti atoms that could trap electrons on the (1 0 0) was arbitrary reduced to represent only 2/3 of the total Ti atoms. Finally, surface localization of electrons is not occurring for the (0 0 1) model[50,84,85], as highlighted before. Therefore, the possible number of active centers should correspond only to holes trapping on the 2f-O atoms. These values are presented in Table 5.

Table 5. The calculated number of 5f-Ti atoms and 2f-O atoms that could act as a trapping center for e^- and h^+, based on the surface structures and trapping process described in the literature.

Surface model	5f-Ti atoms available for e^- trapping ($10^{18}\cdot m^{-2}$)	2f-O atoms available for h^+ trapping ($10^{18}\cdot m^{-2}$)	Refs.
(0 0 1)	0^a	6.96378	[49,50]
(1 0 0)	3.70300^b	5.55450	
(1 0 1)	5.15191	5.15191	

[a] Reported trapping do not occur at the surface

[b] Arbitrary reduced by the 1/3 due to partial delocalization over adjusting 5f-Ti

Based on the obtained number of "active" atoms on the surface, the initial $S\cdot n^{-1}$ ratio was rearranged to the actual number of possible trapping centers (n_{trap}) per number of pollutant molecules (n). Furthermore, the actual number of reacting molecules should differ, depending on its adsorption rate from the fluid to the surface. This process should especially depend on the surface energy (E_{surf}), as it will influence the final energy of adsorption[86]. Therefore, the surface energy was introduced as a final factor in the considered model. Starting from this point, identical analysis was performed; however, the initial $S\cdot n^{-1}$ ratio was changed to the number of different expressions, including either surface energy or calculated $n_{trap}\cdot n^{-1}$ ratio. Therefore, the value on X-axis in Figure 8 was changed, which affected obtained a parameter. Ultimately, new a value was fitted to the trapping energy in the same way as previously. To represent model consistency with the experimental results, the residual sum of squares (RSS) was calculated for each considered model. As presented in Table 6, introduction of different terms either improved or worsened the model's fit, depending on the reaction type. Nevertheless, a visibly better fit can be obtained when specific terms were introduced. Concerning the phenol degradation, introduction of both E_{surf} and the square root of $n_{trap} \cdot n^{-1}$ allowed to achieve the best model accuracy, which especially resulted from the better fit for the high k values.

Table 6. Residual sum of squares (RSS) obtained for the models calculated using different terms in the first step of the fitting.

RSS (10^{-6})	$S \cdot n^{-1}$	$E_{surf} \cdot S \cdot n^{-1}$	$E_{surf}^{2} \cdot S \cdot n^{-1}$	$n_{trap} \cdot n^{-1}$	$E_{surf} \cdot n_{trap} \cdot n^{-1}$	$E_{surf}^{2} \cdot n_{trap} \cdot n^{-1}$	$E_{surf} \cdot (n_{trap} \cdot n^{-1})^{1/2}$
Phenol	0.68	0.71	1.08	0.71	0.67	0.82	**0.14**
Toluene	1.64	1.09	**0.87**	1.90	1.37	**0.90**	2.45

For the toluene degradation reaction, mostly the presence of the second power of E_{surf} improve model accuracy both when $n_{trap} \cdot n^{-1}$ and $S \cdot n^{-1}$ ratios were considered. However, the best fit is still obtained when simple surface area is considered instead of the number of the trapping sites. First of all, this shows that different contributions of the surface energy might be expected for different reaction systems. Especially, it might be suggested that surface energy contributes more to the mass transfer inside the system for the gas phase process, since this reaction was performed in the static air. Secondly, it shows that estimation of the active sites present during the gas phase process is less accurate than for the phenol degradation, This probably results from the difficulties to precisely determine the fraction of the prepared layer, which is freely exposed to the reactions system. Nevertheless, as shown in Figure 11, the general predictions of both models are good, especially in case of phenol degradation. The highest error is observed mostly for the high k values in case of toluene degradation and specifically, this is for the {1 0 1} enclosed octahedral nanoparticles. This suggest that samples enclosed with these facets might behave slightly different than the {1 0 0} and {0 0 1} ones in the gas phase.

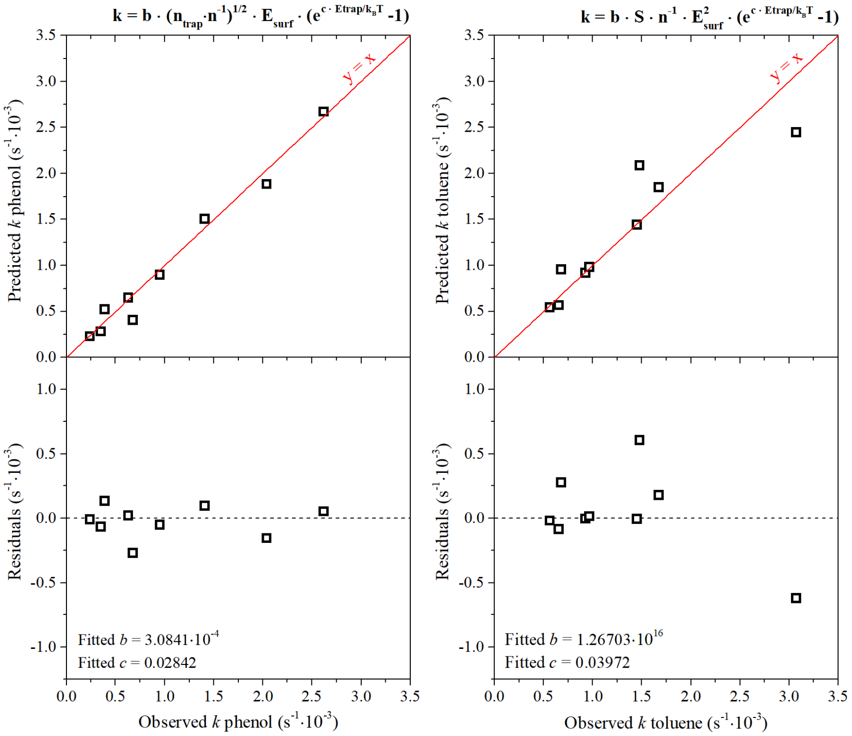

Figure 11. Predicted vs observed *k* and the residual plot for both reactions, obtained with the best-fitting model for both case.

Finally, it could be also noticed that similar behavior was observed for the phenol degradation process. In this case, the introduction of the $E_{surf}\cdot(n_{trap}\cdot n^{-1})^{1/2}$ term produced the best results overall. However, this mainly resulted from the best fit for the high *k* values (so, the octahedral samples), while actually for the low *k*, the relative error was the lowest for the $E_{surf}\cdot n_{trap}\cdot n^{-1}$ term. In fact, the better fit exclusively for the low phenol *k* values is observed even in Figure 10 than in Figure 11.

Ultimately, this suggest that there might be a significant difference in the effect of crucial factors for low and high surface-to-pollutant ratios.

3.5. Side facets effect and variance with different E_{surf} values

The analysis performed so far was focused on the properties of facets, that were found to be dominant for each sample. However, especially in the case of the {0 0 1} and {1 0 0} exposing nanostructures, additional facets must appear at the side/end of the particle to "close" its 3-dimensional structure. These additional side facets are most likely to influence on the final activity, due to the different properties and possible charge separation. Unfortunately, precise description of such facets is difficult when their content is reduced and formation of the strictly defined structures is often not observed. Instead, less defined structures, curvatures, combinations of different facets and microfacets also appear, whose exact structure and properties are not precisely known. In this regard, their systematic introduction into the model is much more complicated than in the case of the dominant facets.

Nevertheless, some simplified approach can be introduced and analyzed, assuming that these side facets would have properties similar to the {1 0 1} one. This could be especially justified by noticing that most of the possible side facets, including structures like {1 0 1}, {1 0 3}, {1 0 5} or {1 1 0}, can expose low-coordinated titanium atoms (4-fold) on the surface, which can especially promote electron trapping. Therefore, possible trapping of the charge carriers should be enhanced if such structures would appear along with the {0 0 1} or {1 0 0} facets. As a result, the E_{trap} value in the model should be increased. This effect can be partially corrected if we assume E_{trap} to be a weighted mean between the dominant facet and the {1 0 1} one, where weights are their approximate share in the particle's surface. Specifically:

$$E_{trap} = E_{dominant} \cdot x_{dominant} + E_{\{1\ 0\ 1\}} \cdot x_{\{1\ 0\ 1\}}$$

where $E_{dominant}$ and $E_{\{101\}}$ are trapping energies reported for the dominant facet and {1 0 1} one respectively, and x are their corresponding share in the particle's surface ($x_{dominant} + x_{\{101\}} = 1$). To obtain x values, detailed analysis of the particles' morphology was performed based on the SEM images and estimated share of the dominant facet was calculated following the observed lengths and theoretical orientation between the (0 0 1)/(1 0 0) and the (1 0 1) crystal planes of anatase (these could be easily obtained from the commonly accessible .cif files). Ultimately, the calculated share of the dominant facets is approx. 80% for the {0 0 1} exposing sample and 82% for the {1 0 0} one. The remainder of the particles is assumed to be enclosed by the {1 0 1} facets in both cases. Based on these values, the modified E_{trap} energy was introduced to the analysis for the best-fitting models, as well as E_{surf} and n_{trap}, recalculated analogically to the trapping energy.

As presented in Figure 12 based on the calculated residuals, such approach gave only a moderate change to the model accuracy, mostly affecting individual points indicated with arrows. Moreover, the effect is opposite for the gas and aqueous phase; that is, for the phenol degradation it improved accuracy while it decreased it for toluene. While this is in some consistency with the previous observations, showing generally that more accurate model is possible to obtain when particles are dispersed in water, more details are probably needed to introduce similar analysis with a significant effect. In this regard, especially more studies on the facet-to-facet junctions would be necessary to precisely describe their interactions in a quantitative way.

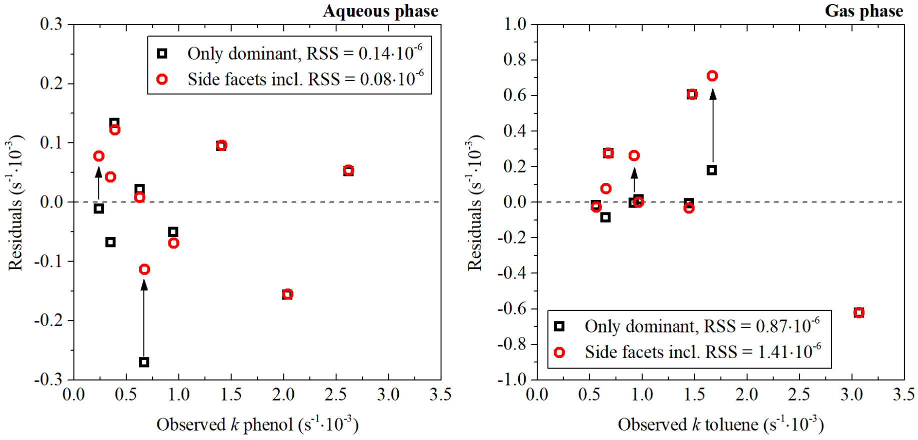

Figure 12. Comparison of the models' accuracy with and without considering possible effect of the side facets for the {0 0 1} and {1 0 0} exposing nanoparticles. Arrows indicate changes most contributing to the total accuracy.

Finally, it was also studied how different values of E_{surf} reported in the literature could affect accuracy of the developed model. To do so, different models were developed, based on the surface energies summarized in Table 7.

Table 7. Different values of surface energy reported in the literature, used for the models' comparison.

Surface energy (J·m^{-2})	Lazzeri *et al.* PBE	Lazzeri *et al.* LDA	Mino *et al.* fixed cell	Mino *et al.* relaxed cell	Arrouvel *et al.*	Zhao *et al.*
{0 0 1}	0.90	1.38	1.275	1.12	0.98	1.08
{1 0 0}	0.53	0.96	0.79	0.76	0.53	0.71
{1 0 1}	0.44	0.84	0.67	0.64	0.44	0.61
Ref.	[49]	[49]	[87]	[87]	[88]	[89]

The change in the model accuracy when developed with different E_{surf} values is presented in Figure 13 as the observed maximum, mean and minimum absolute residual value. Noteworthy, the effect is quite small, with the error change between different models being generally $\leq 5 \cdot 10^{-5}$ s^{-1}. This is approximately 15 % of the lowest rate constants and approx. 5 % of the mean values for both reactions. Moreover, it could be observed that the highest and the lowest errors in the gas phase are almost independent on the surface energy value. Therefore, comparing to previous analysis, the effect is quite small and models with analogical accuracy can be obtained with different E_{surf} values (*e.g.* changes indicated in Figure 12 are generally one order of magnitude higher than here). This is in some general agreement with the known accuracy of the DFT methods, which show that while the exact obtained values could differ between the studies/methods, observed trends are more robust and the change is similar for all considered models. Therefore, as long as the analyzed values are obtained with the same computational details, their effect on the final model is nearly the same.

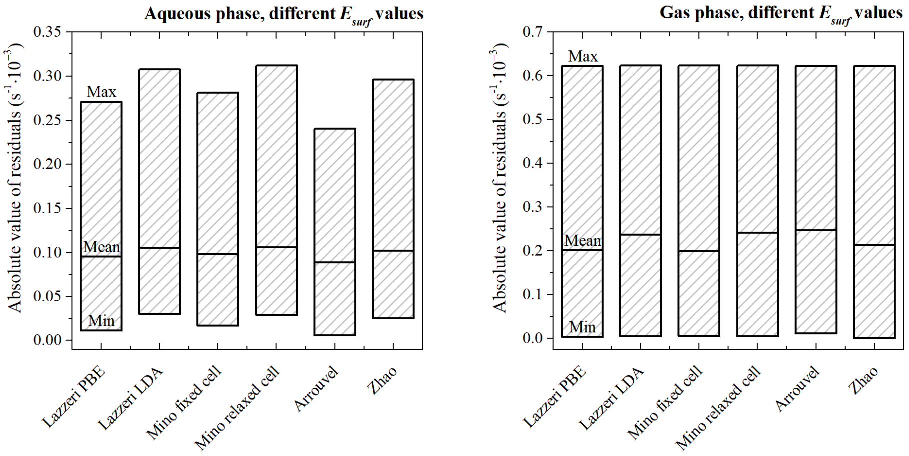

Figure 13. Comparison on absolute error values (maximum, mean and minimum) for models developed with different reported values of surface energy for the dominant facets.

3.6. Fluorination of the {0 0 1} facets and model limitations

Presented analysis showed that activity of the TiO_2 nanostructures in the degradation process of organic compounds is mostly controlled by the charge carriers trapping on the photocatalyst surface. This process is heavily affected by the exposed crystal facet and therefore, through computational analysis of such trapping behavior it is possible to predict activity of the final nanostructure. However, it should be noted that some limitations of such approach are still present. First of all, performed studies are based on the models of ideal surfaces, which under the real conditions are not always expected. For example, fluorination of the {0 0 1} facets was observed during this study as the result of HF-mediated growth. Right now, the presence of different adsorbed species, and fluorine in particular[90–92], is known to affect chemical states on the TiO_2 surface. However it is not arbitrary known how exactly it will affect distribution of the trapped charge carriers. In example, Mino *et al.* have observed that removal of the fluorine from the {0 0 1} facets by NaOH washing increased phenol degradation rate[80]. On the other hand it should be also noted, that some surface fluorination is known to increase ·OH generation through water oxidation by the TiO_2, as shown in example by Chen *et al.*[93] or Mrowetz *et al.*[94] Therefore, at this point it could be expected that some maximum activity of the {0 0 1} facets should be observed, depending on the exact presence of the fluorine, however the optimal conditions for each specific case is more complex. In this regard, to increase the observed activity of the prepared {0 0 1} nanosheets different washing procedures were performed, including: (1) washing with a 0.1 M NaOH solution for 2 h at 300 K, with TiO_2 concentration of 10 $mg \cdot cm^{-3}$, followed by rising with 0.1 M HNO_3 and water, as described by Mino *et al.*[80]; (2) analogical procedure but only with 30 min of NaOH wash; (3) analogical to 1, but without HNO_3 washing; (4) analogical to 1, but without HNO_3 washing and with NaOH concentration reduced to 0.05 M; (5) only single-time rinsing with 0.1 M NaOH solution and then with water. Performed activity tests after the washing procedures are presented in Figure 14 for the degradation of 20 mg·dm^{-3} phenol solution (analogical effects was observed for other reactions).

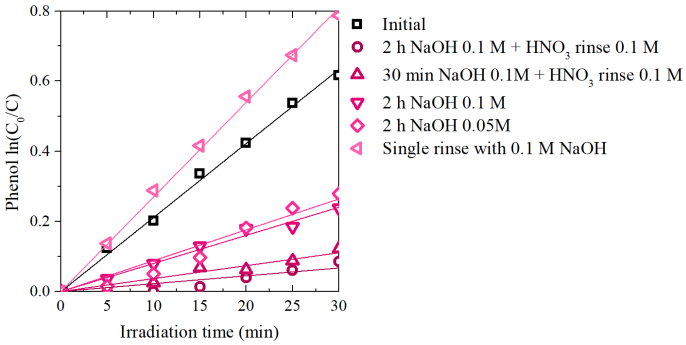

Figure 14. Effect of different washing procedures on the observed photocatalytic activity of the anatase particles with exposed {0 0 1} facets in the degradation of 20 mg·dm^{-3} phenol solution.

It was found that the activity increases only in the case of procedure 5, i.e., single-time rinsing with 0.1 M NaOH solution and then with water, while all other procedures lead to a reduction of the observed activity. This suggests that the exact surface states became alternated between different washing procedures. Nevertheless, the activity of the {0 0 1} facets could be indeed increased by eliminating some of the present fluorine and the final activity is approximately 28 % higher than initial, which is comparable with the effect observed by Mino *et al.*[80] This change affected model details and generally resulted in lower accuracy of all considered models. Nevertheless, the change is not high enough to change the general observations. Specifically, the relative activity of different facets remain the same and still show good exponential correlation with a trapping energy. Finally, the “best-fitting” models from Table 6 remain best-fitting after the washing and their comparison is shown in Table 8.

Table 8. Effect of washing the {0 0 1} nanosheets with NaOH solution on the details of the best-fitting models for both reactions.

	Aqueous phase		Gas phase	
	Before wash	After wash	Before wash	After wash
Fitted a for {0 0 1} series	$3.18858\cdot10^{-4}$	$4.0763\cdot10^{-4}$	$1.34236\cdot10^{16}$	$1.71608\cdot10^{16}$
R^2 exp fit of a for all series	0.9985	0.99495	0.99957	0.99993
Fitted b	$3.0841\cdot10^{-4}$	$3.32709\cdot10^{-4}$	$1.26703\cdot10^{16}$	$1.29706\cdot10^{16}$
Fitted c	0.02842	0.02766	0.03972	0.03948
RSS (10^{-6})	0.14	0.28	0.87	1.03

The second challenge of the presented model is that performed analysis does not represent total reactivity of the charge carriers, since their direct transfer from the photocatalysts, without trapping, is still possible[95]. This leads to the problem that it is not possible to precisely determine the “limiting” current of the specific charge carrier[96,97], in example e^- reacting on the {0 0 1} facet. This problem is observed both for pure, as well as for the fluorinated (0 0 1) surfaces. The second one was specifically performed during this study and obtained results of the possible electron trapping on the F-terminated (0 0 1) model are presented in Figure 15, based on the density of states (DOS) distribution. As shown in Figure 15b, no change in the DOS position is observed after localizing electron on the surface Ti, which show that no additional states are formed. Moreover, calculated Bader charge on the trapping Ti atom indicated only partial localization, comparing to the delocalized model (0.16e difference, where e is the electron charge unit). Finally, trapping energy, defined analogical as in the work of Ma *et al.*[50] resulted only in a value of 2 meV. Therefore, possible energetic stabilization due to charge localization is negligible and below DFT accuracy. In this regard, further studies are needed on the possible electron transfer and its reactivity on the (0 0 1) surface, as well as on the effect of the fluorine or other adsorbates on this particular process. The presented approach allows only to predict relative reactivity of different surfaces based on their comparison, rather than arbitrary model it from the single simulation.

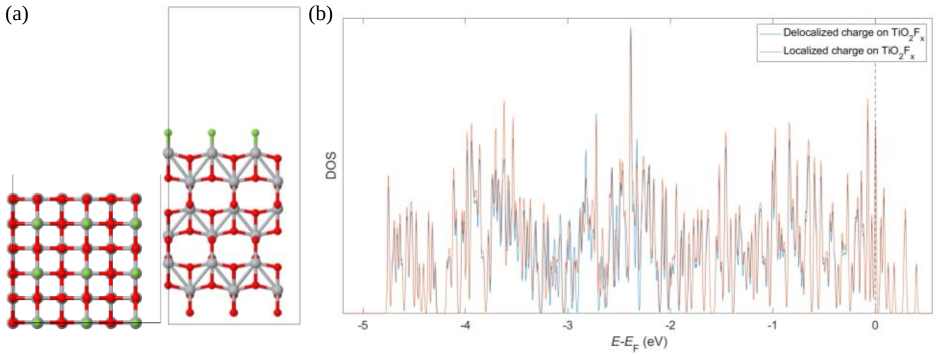

Figure 15. (a) Top and side views of the model of the F-covered anatase TiO_2 (0 0 1) surface. The rectangle represents the boundaries of the periodic simulation box, and circles represent atoms of titanium (grey), oxygen (red) or fluorine (green). (b) Density of states (DOS) plot of the TiO_2 system in its negatively charged state, with the charge of the extra electron localized or delocalized. The energies are relative to the Fermi level, represented by the dashed vertical line.

Thus, it is expected that the specific details of the model should also depend on the exact nature of the pollutant. At this point, we can anticipate that pollutants which prefer to directly transfer an electron to the photocatalyst (*e.g.* some dyes) would show higher deviation from the model introduced in this work.

Nevertheless, as the part of advanced oxidation technologies, application of the highly active photocatalysts such as TiO_2, is connected with the degradation of compounds, which are photochemically stable and their degradation must be initiated by the reactive species generated in the system. In such cases, phenol and toluene are suggested as good model representatives.

Moreover, presented analysis can still provide valuable information about the photocatalyst. It allows to show if trapped charge carriers are mostly responsible for inducing the degradation reaction. In such case, the number of reacting species depends on the trapping energy (the energy gain of the system when the charge carrier became trapped on the surface) rather than surface energy or even the number of active sites (undercoordinated atoms). Since design strategies of the possibly most active photocatalysts still present an extremely complex image, such findings might be a good guide for future studies. Above all this directly links observed photocatalytic activity to the specific surface features that could be designed, simulate and optimized without extensive experimental work. So far, such approach is still generally missing in the literature.

4. CONCLUSIONS

Analyzed data showed that under the accepted experimental conditions, photocatalytic degradation of both toluene and phenol is mainly affected by the energy of charge carriers trapping at the photocatalysts' surface. This straightforward predicts the highest per-surface photocatalytic activity of the {1 0 1} enclosed anatase octahedrons, due to their high trapping energy. Simultaneously, anatase nanosheets with the {0 0 1} exposed facets are the least active ones. The relation between trapping energy and observed rate constants is exponential, which is in accordance with the expected Boltzmann distribution of the trapped states. However, the exact value of the E_{trap}/kT exponent should be further weighted with additional parameter c. It could be suggested that this parameter represents the fraction of the surface-trapped states that effectively induce the process, since it is well known that not all excited/trapped charge carriers will contribute to the final reaction. Moreover, the c value obtained during analyses was always found to be in the range of 0.020-0.041, which would fit the value of, *e.g.* photonic efficiency of ·OH generation (approx. 3%). Concerning other possible factors, their introduction might further improve performed prediction. However, their contribution depends on the reaction system.

For the phenol degradation, surface energy affects the rate constant linearly, while in the gas-phase reaction, it acts as a E_{surf}^2. Finally, depending on the reaction, the best model was obtained when the number of possible trapping centers was introduced (water phase) or it was estimated with the simple surface area of the photocatalyst (gas phase). These results might be beneficial for further design of the new photocatalyst structures, giving a clear insight on what effect might be expected for its different surfaces without performing extensive experimental studies.

ACKNOWLEDGMENTS

The research was financially supported by the Polish National Science Centre (grant no. NCN 2018/30/E/ST5/00845). SD is grateful for the financial support from the Gdansk University of Technology (program POWR.03.05.00-00-Z044/17), and by project CICECO-Aveiro Institute of Materials with references UIDB/50011/2020, UIDP/50011/2020 and LA/P/0006/2020 financed by national funds through the Fundação para a Ciência e a Tecnologia (FCT/MCTES) and co-financed by FEDER under the PT2020 Partnership Agreement.

REFERENCES

(1) Fujishima, A.; Honda, K. Electrochemical Photolysis of Water at a Semiconductor Electrode. *Nature* **1972**, *238*, 37–38.

(2) Domen, K.; Naito, S.; Soma, M.; Onishi, T.; Tamaru, K. Photocatalytic Decomposition of Water Vapour on an NiO-SrTiO3 Catalyst. *J. Chem. Soc. Chem. Commun.* **1980**, No. 12, 543–544.

(3) Kraeutler, B.; Bard, A. J. Heterogeneous Photocatalytic Decomposition of Saturated

Carboxylic Acids on TiO2 Powder. Decarboxylative Route to Alkanes. *J. Am. Chem. Soc.* **1978**, *100*, 5985–5992.

(4) Yoneyama, H.; Yamashita, Y.; Tamura, H. Heterogeneous Photocatalytic Reduction of Dichromate on N-Type Semiconductor Catalysts. *Nature*. 1979, *282*, 817–818.

(5) *Photocatalysis: Fundamentals, Materials and Potential*; Pichat, P., Ed.; MDPI, Basel, 2016.

(6) *Heterogeneous Photocatalysis. From Fundamentals to Green Applications*; Colmenares, J. C., Xu, Y.-J., Eds.; Springer Berlin, Heidelberg, 2016.

(7) *Photocatalysis and Water Purification. From Fundamentals to Recent Applic*; Pichat, P., Ed.; Viley-VCH, Weinheim, 2013.

(8) Takata, T.; Jiang, J.; Sakata, Y.; Nakabayashi, M.; Shibata, N.; Nandal, V.; Seki, K.; Hisatomi, T.; Domen, K. Photocatalytic Water Splitting with a Quantum Efficiency of Almost Unity. *Nature* **2020**, *581*, 411–414.

(9) Moniz, S. J. A.; Shevlin, S. A.; Martin, D. J.; Guo, Z. X.; Tang, J. Visible-Light Driven Heterojunction Photocatalysts for Water Splitting-a Critical Review. *Energy Environ. Sci.* **2015**, *8*, 731–759.

(10) Meng, A.; Zhang, J.; Xu, D.; Cheng, B.; Yu, J. Enhanced Photocatalytic H2-Production Activity of Anatase TiO2 Nanosheet by Selectively Depositing Dual-Cocatalysts on (101) and (001) Facets. *Appl. Catal. B Environ.* **2016**, *198*, 286–294.

(11) Simon, T.; Carlson, M. T.; Stolarczyk, J. K.; Feldmann, J. Electron Transfer Rate vs Recombination Losses in Photocatalytic H2 Generation on Pt- Decorated CdS Nanorods. *ACS Energy Lett.* **2016**, *1*, 1137–1142.

(12) Xie, S.; Zhang, Q.; Liu, G.; Wang, Y. Photocatalytic and Photoelectrocatalytic Reduction of CO2 Using Heterogeneous Catalysts with Controlled Nanostructures. *Chem. Commun.*

2016, *52*, 35-59.

(13) Liu, X.; Ye, L.; Liu, S.; Li, Y.; Ji, X. Photocatalytic Reduction of CO2 by ZnO Micro/Nanomaterials with Different Morphologies and Ratios of {0001} Facets. *Sci. Rep.* **2016**, *6*, 1–9.

(14) Alshaikh, H.; Al-Hajji, L. A.; Mahmoud, M. H. H.; Ismail, A. A. Visible-Light-Driven S-Scheme Mesoporous Ag3VO4 /C3N4 Heterojunction with Promoted Photocatalytic Performances. *Sep. Purif. Technol.* **2021**, *272*, No. 118914.

(15) Grzegórska, A.; Głuchowski, P.; Karczewski, J.; Ryl, J.; Wysocka, I.; Siuzdak, K.; Trykowski, G.; Grochowska, K.; Zielińska-Jurek, A. Enhanced Photocatalytic Activity of Accordion-like Layered Ti3C2 (MXene) Coupled with Fe-Modified Decahedral Anatase Particles Exposing {1 0 1} and {0 0 1} Facets. *Chem. Eng. J.* **2021**, *426*, No. 130801.

(16) Sulowska, A.; Wysocka, I.; Pelczarski, D.; Karczewski, J.; Zielińska-Jurek, A. Hybrid TiO2-Polyaniline Photocatalysts and Their Application in Building Gypsum Plasters. *Materials (Basel).* **2020**, *13*, No. 1516.

(17) Wang, K.; Bielan, Z.; Endo-Kimura, M.; Janczarek, M.; Zhang, D.; Kowalski, D.; Zielińska-Jurek, A.; Markowska-Szczupak, A.; Ohtani, B.; Kowalska, E. On the Mechanism of Photocatalytic Reactions on CuxO@TiO$_2$ core-shell Photocatalysts. *J. Mater. Chem. A* **2021**, *9*, 10135–10145.

(18) Kowalkińska, M.; Głuchowski, P.; Swebocki, T.; Ossowski, T.; Ostrowski, A.; Bednarski, W.; Karczewski, J.; Zielińska-Jurek, A. Scheelite-Type Wide-Bandgap ABO$_4$ Compounds (A = Ca, Sr, and Ba; B = Mo and W) as Potential Photocatalysts for Water Treatment. *J. Phys. Chem. C* **2021**, *125*, 25497-25513.

(19) Yang, J.; Yan, H.; Wang, X.; Wen, F.; Wang, Z.; Fan, D.; Shi, J.; Li, C. Roles of Cocatalysts

in Pt-PdS/CdS with Exceptionally High Quantum Efficiency for Photocatalytic Hydrogen Production. *J. Catal.* **2012**, *290*, 151–157.

(20) She, X.; Wu, J.; Zhong, J.; Xu, H.; Yang, Y.; Vajtai, R.; Lou, J.; Liu, Y.; Du, D.; Li, H.; Ajayan, P. M. Oxygenated Monolayer Carbon Nitride for Excellent Photocatalytic Hydrogen Evolution and External Quantum Efficiency. *Nano Energy* **2016**, *27*, 138–146.

(21) Hazra, C.; Samanta, T.; Asaithambi, A. V.; Mahalingam, V. Bilayer Stabilized Ln3+-Doped CaMoO4 Nanocrystals with High Luminescence Quantum Efficiency and Photocatalytic Properties. *Dalt. Trans.* **2014**, *43*, 6623–6630.

(22) Guo, H. L.; Du, H.; Jiang, Y. F.; Jiang, N.; Shen, C. C.; Zhou, X.; Liu, Y. N.; Xu, A. W. Artificial Photosynthetic Z-Scheme Photocatalyst for Hydrogen Evolution with High Quantum Efficiency. *J. Phys. Chem. C* **2017**, *121*, 107–114.

(23) Li, X.; Yu, J.; Jaroniec, M. Hierarchical Photocatalysts. *Chem. Soc. Rev.* **2016**, *45*, 2603–2636.

(24) Idrees, M.; Din, H. U.; Rehman, S. U.; Shafiq, M.; Saeed, Y.; Bui, H. D.; Nguyen, C. V.; Amin, B. Electronic Properties and Enhanced Photocatalytic Performance of van Der Waals Heterostructures of ZnO and Janus Transition Metal Dichalcogenides. *Phys. Chem. Chem. Phys.* **2020**, *22*, 10351–10359.

(25) Schneider, J.; Matsuoka, M.; Takeuchi, M.; Zhang, J.; Horiuchi, Y.; Anpo, M.; Bahnemann, D. W. Understanding TiO2 Photocatalysis: Mechanisms and Materials. *Chem. Rev.* **2014**, *114*, 9919–9986.

(26) Zhang, J.; Zhou, P.; Liu, J.; Yu, J. New Understanding of the Difference of Photocatalytic Activity among Anatase, Rutile and Brookite TiO2. *Phys. Chem. Chem. Phys.* **2014**, *16*, 20382–20386.

(27) Radecka, M.; Rekas, M.; Trenczek-Zajac, A.; Zakrzewska, K. Importance of the Band Gap Energy and Flat Band Potential for Application of Modified TiO2 Photoanodes in Water Photolysis. *J. Power Sources* **2008**, *181*, 46–55.

(28) Nosaka, Y.; Nosaka, A. Y. Understanding Hydroxyl Radical (•OH) Generation Processes in Photocatalysis. *ACS Energy Lett.* **2016**, *1*, 356–359.

(29) Wang, C.; Zhang, X.; Liu, Y. Promotion of Multi-Electron Transfer for Enhanced Photocatalysis: A Review Focused on Oxygen Reduction Reaction. *Appl. Surf. Sci.* **2015**, *358*, 28–45.

(30) Bianco Prevot, A.; Vincenti, M.; Bianciotto, A.; Pramauro, E. Photocatalytic and Photolyric Transformation of Chloramben in Aqueous Solutions. *Appl. Catal. B Environ.* **1999**, *22*, 149-158.

(31) Poulios, I.; Kositzi, M.; Kouras, A. Photocatalytic Decomposition of Triclopyr over Aqueous Semiconductor Suspensions. *J. Photochem. Photobiol. A Chem.* **1998**, *115*, 175–183.

(32) Lair, A.; Ferronato, C.; Chovelon, J. M.; Herrmann, J. M. Naphthalene Degradation in Water by Heterogeneous Photocatalysis: An Investigation of the Influence of Inorganic Anions. *J. Photochem. Photobiol. A Chem.* **2008**, *193*, 193–203.

(33) Dudziak, S.; Bielan, Z.; Kubica, P.; Zielinska-Jurek, A. Optimization of Carbamazepine Photodegradation on Defective TiO2-Based Magnetic Photocatalyst. *J. Environ. Chem. Eng.* **2021**, *9*, No. 105782.

(34) Sun, L.; Shao, R.; Chen, Z.; Tang, L.; Dai, Y.; Ding, J. Alkali-Dependent Synthesis of Flower-like ZnO Structures with Enhanced Photocatalytic Activity via a Facile Hydrothermal Method. *Appl. Surf. Sci.* **2012**, *258*, 5455–5461.

(35) Chen, Y. J.; Chiang, Y. W.; Huang, M. H. Synthesis of Diverse Ag2O Crystals and Their Facet-Dependent Photocatalytic Activity Examination. *ACS Appl. Mater. Interfaces* **2016**, *8*, 19672–19679.

(36) Cho, C. H.; Kim, D. K.; Kim, D. H. Photocatalytic Activity of Monodispersed Spherical TiO2 Particles with Different Crystallization Routes. *J. Am. Ceram. Soc.* **2003**, *86*, 1138–1145.

(37) Wang, X.; Sø, L.; Su, R.; Wendt, S.; Hald, P.; Mamakhel, A.; Yang, C.; Huang, Y.; Iversen, B. B.; Besenbacher, F. The Influence of Crystallite Size and Crystallinity of Anatase Nanoparticles on the Photo-Degradation of Phenol. *J. Catal.* **2014**, *310*, 100–108.

(38) Kowalkińska, M.; Dudziak, S.; Karczewski, J.; Ryl, J.; Trykowski, G.; Zielińska-Jurek, A. Facet Effect of TiO2 Nanostructures from TiOF2 and Their Photocatalytic Activity. *Chem. Eng. J.* **2021**, *404*, No. 126493.

(39) Pan, J.; Liu, G.; Lu, G. Q.; Cheng, H. M. On the True Photoreactivity Order of {001}, {010}, and {101} Facets of Anatase TiO2 Crystals. *Angew. Chemie - Int. Ed.* **2011**, *50*, 2133–2137.

(40) Gordon, T. R.; Cargnello, M.; Paik, T.; Mangolini, F.; Weber, R. T.; Fornasiero, P.; Murray, C. B. Nonaqueous Synthesis of TiO2 Nanocrystals Using TiF4 to Engineer Morphology, Oxygen Vacancy Concentration, and Photocatalytic Activity. *J. Am. Chem. Soc.* **2012**, *134*, 6751–6761.

(41) Günnemann, C.; Haisch, C.; Fleisch, M.; Schneider, J.; Emeline, A. V.; Bahnemann, D. W. Insights into Different Photocatalytic Oxidation Activities of Anatase, Brookite, and Rutile Single-Crystal Facets. *ACS Catal.* **2019**, *9*, 1001–1012.

(42) Dudziak, S.; Kowalkińska, M.; Karczewski, J.; Pisarek, M.; Siuzdak, K.; Kubiak, A.;

Siwińska-Ciesielczyk, K.; Zielińska-Jurek, A. Solvothermal Growth of {0 0 1} Exposed Anatase Nanosheets and Their Ability to Mineralize Organic Pollutants. The Effect of Alcohol Type and Content on the Nucleation and Growth of TiO2 Nanostructures. *Appl. Surf. Sci.* **2021**, *563*, No. 150360.

(43) Li, M.; Chen, Y.; Li, W.; Li, X.; Tian, H.; Wei, X.; Ren, Z.; Han, G. Ultrathin Anatase TiO2 Nanosheets for High-Performance Photocatalytic Hydrogen Production. *Small* **2017**, *13,* No. 1604115.

(44) Wen, C. Z.; Zhou, J. Z.; Jiang, H. B.; Hu, Q. H.; Qiao, S. Z.; Yang, H. G. Synthesis of Micro-Sized Titanium Dioxide Nanosheets Wholly Exposed with High-Energy {001} and {100} Facets. *Chem. Commun.* **2011**, *47*, 4400–4402.

(45) Yuan, Y. J.; Ye, Z. J.; Lu, H. W.; Hu, B.; Li, Y. H.; Chen, D. Q.; Zhong, J. S.; Yu, Z. T.; Zou, Z. G. Constructing Anatase TiO2 Nanosheets with Exposed (001) Facets/Layered MoS2 Two-Dimensional Nanojunctions for Enhanced Solar Hydrogen Generation. *ACS Catal.* **2016**, *6*, 532–541.

(46) Zhang, D.; Wang, S.; Zhu, J.; Li, H.; Lu, Y. WO3 Nanocrystals with Tunable Percentage of (001)-Facet Exposure. *Appl. Catal. B Environ.* **2012**, *123–124*, 398–404.

(47) Amano, F.; Yasumoto, T.; Prieto-Mahaney, O. O.; Uchida, S.; Shibayama, T.; Ohtani, B. Photocatalytic Activity of Octahedral Single-Crystalline Mesoparticles of Anatase Titanium(IV) Oxide. *Chem. Commun.* **2009**, 2311–2313.

(48) Li, J.; Xu, D. Tetragonal Faceted-Nanorods of Anatase TiO2 Single Crystals with a Large Percentage of Active {100} Facets. *Chem. Commun.* **2010**, *46*, 2301–2303.

(49) Lazzeri, M.; Vittadini, A.; Selloni, A. Structure and Energetics of Stoichiometric TiO2 Anatase Surfaces. *Phys. Rev. B - Condens. Matter Mater. Phys.* **2001**, *63*, 1554091–

1554099.

(50) Ma, X.; Dai, Y.; Guo, M.; Huang, B. Relative Photooxidation and Photoreduction Activities of the {100}, {101}, and {001} Surfaces of Anatase TiO2. *Langmuir* **2013**, *29*, 13647–13654.

(51) Amano, F.; Nogami, K.; Tanaka, M.; Ohtani, B. Correlation between Surface Area and Photocatalytic Activity for Acetaldehyde Decomposition over Bismuth Tungstate Particles with a Hierarchical Structure. *Langmuir* **2010**, *26*, 7174–7180.

(52) Chiou, C. H.; Wu, C. Y.; Juang, R. S. Influence of Operating Parameters on Photocatalytic Degradation of Phenol in UV/TiO2 Process. *Chem. Eng. J.* **2008**, *139*, 322–329.

(53) Zhang, C.; Hu, P.; Alavi, A. A General Mechanism for CO Oxidation on Close-Packed Transition Metal Surfaces. *J. Am. Chem. Soc.* **1999**, *121*, 7931–7932.

(54) Deskins, N. A.; Rousseau, R.; Dupuis, M. Localized Electronic States from Surface Hydroxyls and Polarons in TiO 2(110). *J. Phys. Chem. C* **2009**, *113*, 14583–14586.

(55) Deskins, N. A.; Dupuis, M. Intrinsic Hole Migration Rates in TiO2 from Density Functional Theory. *J. Phys. Chem. C* **2009**, *113*, 346–358.

(56) Deskins, N. A.; Dupuis, M. Electron Transport via Polaron Hopping in Bulk TiO2: A Density Functional Theory Characterization. *Phys. Rev. B* **2007**, *75*, 1–10.

(57) Han, X.; Kuang, Q.; Jin, M.; Xie, Z.; Zheng, L. Synthesis of Titania Nanosheets with High Percentage of Exposed (001) Facets and Related Photocatalytic Properties. *J. Am. Chem. Soc.* **2009**, *131*, 3152–3153.

(58) Yu, J.; Fan, J.; Lv, K. Anatase TiO2 Nanosheets with Exposed (001) Facets: Improved Photoelectric Conversion Efficiency in Dye-Sensitized Solar Cells. *Nanoscale* **2010**, *2*, 2144–2149.

(59) Zhang, Y.; Li, C.; Pan, C. N + Ni Codoped Anatase TiO2 Nanocrystals with Exposed {001} Facets through Two-Step Hydrothermal Route. *J. Am. Ceram. Soc.* **2012**, *95*, 2951–2956.

(60) Mao, J.; Ye, L.; Li, K.; Zhang, X.; Liu, J.; Peng, T.; Zan, L. Pt-Loading Reverses the Photocatalytic Activity Order of Anatase TiO2 {001} and {010} Facets for Photoreduction of CO2 to CH4. *Appl. Catal. B Environ.* **2014**, *144*, 855–862.

(61) Huang, Z.; Wang, Z.; Lv, K.; Zheng, Y.; Deng, K. Transformation of TiOF2 Cube to a Hollow Nanobox Assembly from Anatase TiO2 Nanosheets with Exposed {001} Facets via Solvothermal Strategy. *ACS Appl. Mater. Interfaces* **2013**, *5*, 8663–8669.

(62) Yu, J.; Qi, L.; Jaroniec, M. Hydrogen Production by Photocatalytic Water Splitting over Pt/TiO 2 Nanosheets with Exposed (001) Facets. *J. Phys. Chem. C* **2010**, *114*, 13118–13125.

(63) Wang, Z.; Lv, K.; Wang, G.; Deng, K.; Tang, D. Study on the Shape Control and Photocatalytic Activity of High-Energy Anatase Titania. *Appl. Catal. B Environ.* **2010**, *100*, 378–385.

(64) Wei, Z.; Kowalska, E.; Verrett, J.; Colbeau-Justin, C.; Remita, H.; Ohtani, B. Morphology-Dependent Photocatalytic Activity of Octahedral Anatase Particles Prepared by Ultrasonication-Hydrothermal Reaction of Titanates. *Nanoscale* **2015**, *7*, 12392–12404.

(65) Gai, L.; Mei, Q.; Qin, X.; Li, W.; Jiang, H.; Duan, X. Controlled Synthesis of Anatase TiO2 Octahedra with Enhanced Photocatalytic Activity. *Mater. Res. Bull.* **2013**, *48*, 4469–4475.

(66) Li, R.; Zhang, X.; Dong, H.; Li, Q.; Shuai, Z.; Hu, W. Gibbs-Curie-Wulff Theorem in Organic Materials: A Case Study on the Relationship between Surface Energy and Crystal Growth. *Adv. Mater.* **2016**, *28*, 1697–1702.

(67) Yang, H. G.; Sun, C. H.; Qiao, S. Z.; Zou, J.; Liu, G.; Smith, S. C.; Cheng, H. M.; Lu, G.

Q. Anatase TiO2 Single Crystals with a Large Percentage of Reactive Facets. *Nature* **2008**, *453*, 638–641.

(68) Yang, H. G.; Liu, G.; Qiao, S. Z.; Sun, C. H.; Jin, Y. G.; Smith, S. C.; Zou, J.; Cheng, H. M.; Lu, G. Q. Solvothermal Synthesis and Photoreactivity of Anatase TiO2 Nanosheets with Dominant {001} Facets. *J. Am. Chem. Soc.* **2009**, *131*, 4078–4083.

(69) Barnard, A. S.; Curtiss, L. A. Prediction of TiO2 Nanoparticle Phase and Shape Transitions Controlled by Surface Chemistry. *Nano Lett.* **2005**, *5*, 1261–1266.

(70) Zhu, J.; Lv, F.; Xiao, S.; Bian, Z.; Buntkowsky, G.; Nuckolls, C.; Li, H. Covalent Attachment and Growth of Nanocrystalline Films of Photocatalytic TiOF2. *Nanoscale* **2014**, *6*, 14648–14651.

(71) Yu, J. C.; Yu, J.; Ho, W.; Jiang, Z.; Zhang, L. Effects of F- Doping on the Photocatalytic Activity and Microstructures of Nanocrystalline TiO2 Powders. *Chem. Mater.* **2002**, *14*, 3808–3816.

(72) Ruzicka, J. Y.; Bakar, F. A.; Thomsen, L.; Cowie, B. C.; McNicoll, C.; Kemmitt, T.; Brand, H. E. A.; Ingham, B.; Andersson, G. G.; Golovko, V. B. XPS and NEXAFS Study of Fluorine Modified TiO2 Nano-Ovoids Reveals Dependence of Ti3+ Surface Population on the Modifying Agent. *RSC Adv.* **2014**, *4*, 20649–20658.

(73) Seo, M. H.; Yuasa, M.; Kida, T.; Huh, J. S.; Shimanoe, K.; Yamazoe, N. Gas Sensing Characteristics and Porosity Control of Nanostructured Films Composed of TiO2 Nanotubes. *Sensors Actuators, B Chem.* **2009**, *137*, 513–520.

(74) Nosaka, Y.; Nosaka, A. Y. Generation and Detection of Reactive Oxygen Species in Photocatalysis. *Chem. Rev.* **2017**, *117*, 11302–11336.

(75) Hirakawa, T.; Yawata, K.; Nosaka, Y. Photocatalytic Reactivity for O2·- and OH· Radical

Formation in Anatase and Rutile TiO2 Suspension as the Effect of H2O2 Addition. *Appl. Catal. A Gen.* **2007**, *325*, 105–111.

(76) René, A.; Abasq, M. L.; Hauchard, D.; Hapiot, P. How Do Phenolic Compounds React toward Superoxide Ion? A Simple Electrochemical Method for Evaluating Antioxidant Capacity. *Anal. Chem.* **2010**, *82*, 8703–8710.

(77) Marugán, J.; Hufschmidt, D.; López-Muñoz, M. J.; Selzer, V.; Bahnemann, D. Photonic Efficiency for Methanol Photooxidation and Hydroxyl Radical Generation on Silica-Supported TiO2 Photocatalysts. *Appl. Catal. B Environ.* **2006**, *62*, 201–207.

(78) Shirai, K.; Fazio, G.; Sugimoto, T.; Selli, D.; Ferraro, L.; Watanabe, K.; Haruta, M.; Ohtani, B.; Kurata, H.; Di Valentin, C.; Matsumoto, Y. Water-Assisted Hole Trapping at the Highly Curved Surface of Nano-TiO2 Photocatalyst. *J. Am. Chem. Soc.* **2018**, *140*, 1415–1422.

(79) Chen, J.; Li, Y. F.; Sit, P.; Selloni, A. Chemical Dynamics of the First Proton-Coupled Electron Transfer of Water Oxidation on TiO2 Anatase. *J. Am. Chem. Soc.* **2013**, *135*, 18774–18777.

(80) Mino, L.; Pellegrino, F.; Rades, S.; Radnik, J.; Hodoroaba, V. D.; Spoto, G.; Maurino, V.; Martra, G. Beyond Shape Engineering of TiO2 Nanoparticles: Post-Synthesis Treatment Dependence of Surface Hydration, Hydroxylation, Lewis Acidity and Photocatalytic Activity of TiO2 Anatase Nanoparticles with Dominant {001} or {101} Facets. *ACS Appl. Nano Mater.* **2018**, *1*, 5355–5365.

(81) Litke, A.; Su, Y.; Tranca, I.; Weber, T.; Hensen, E. J. M.; Hofmann, J. P. Role of Adsorbed Water on Charge Carrier Dynamics in Photoexcited TiO2. *J. Phys. Chem. C* **2017**, *121*, 7514–7524.

(82) Hwang, J. Y.; Moon, G. hee; Kim, B.; Tachikawa, T.; Majima, T.; Hong, S.; Cho, K.; Kim,

W.; Choi, W. Crystal Phase-Dependent Generation of Mobile OH Radicals on TiO2: Revisiting the Photocatalytic Oxidation Mechanism of Anatase and Rutile. *Appl. Catal. B Environ.* **2021**, *286*, No. 119905.

(83) Setvin, M.; Aschauer, U.; Hulva, J.; Simschitz, T.; Daniel, B.; Schmid, M.; Selloni, A.; Diebold, U. Following the Reduction of Oxygen on TiO2 Anatase (101) Step by Step. *J. Am. Chem. Soc.* **2016**, *138*, 9565–9571.

(84) Selcuk, S.; Selloni, A. Facet-Dependent Trapping and Dynamics of Excess Electrons at Anatase TiO2 Surfaces and Aqueous Interfaces. *Nat. Mater.* **2016**, *15*, 1107–1112.

(85) Carey, J. J.; McKenna, K. P. Does Polaronic Self-Trapping Occur at Anatase TiO2 Surfaces? *J. Phys. Chem. C* **2018**, *122*, 27540–27553.

(86) Bahamon, D.; Khalil, M.; Belabbes, A.; Alwahedi, Y.; Vega, L. F.; Polychronopoulou, K. A DFT Study of the Adsorption Energy and Electronic Interactions of the SO2 molecule on a CoP Hydrotreating Catalyst. *RSC Adv.* **2021**, *11*, 2947–2957.

(87) Mino, L.; Ferrari, A. M.; Lacivita, V.; Spoto, G.; Bordiga, S.; Zecchina, A. CO Adsorption on Anatase Nanocrystals: A Combined Experimental and Periodic DFT Study. *J. Phys. Chem. C* **2011**, *115*, 7694–7700.

(88) Arrouvel, C.; Digne, M.; Breysse, M.; Toulhoat, H.; Raybaud, P. Effects of Morphology on Surface Hydroxyl Concentration: A DFT Comparison of Anatase-TiO2 and γ-Alumina Catalytic Supports. *J. Catal.* **2004**, *222*, 152–166.

(89) Zhao, Z.; Li, Z.; Zou, Z. Surface Properties and Electronic Structure of Low-Index Stoichiometric Anatase TiO2 Surfaces. *J. Phys. Condens. Matter* **2010**, *22*, No. 175008.

(90) Seo, H.; Baker, L. R.; Hervier, A.; Kim, J.; Whitten, J. L.; Somorjai, G. A. Generation of Highly N-Type Titanium Oxide Using Plasma Fluorine Insertion. *Nano Lett.* **2011**, *11*, 751–

756.

(91) Pellegrino, F.; Morra, E.; Mino, L.; Martra, G.; Chiesa, M.; Maurino, V. Surface and Bulk Distribution of Fluorides and Ti3+ Species in TiO2 Nanosheets: Implications on Charge Carrier Dynamics and Photocatalysis. *J. Phys. Chem. C* **2020**, *124*, 3141–3149.

(92) Peng, Y. K.; Keeling, B.; Li, Y.; Zheng, J.; Chen, T.; Chou, H. L.; Puchtler, T. J.; Taylor, R. A.; Tsang, S. C. E. Unravelling the Key Role of Surface Features behind Facet-Dependent Photocatalysis of Anatase TiO2. *Chem. Commun.* **2019**, *55*, 4415–4418.

(93) Chen, M.; Ma, J.; Zhang, B.; He, G.; Li, Y.; Zhang, C.; He, H. Remarkable Synergistic Effect between {001} Facets and Surface F Ions Promoting Hole Migration on Anatase TiO2. *Appl. Catal. B Environ.* **2017**, *207*, 397–403.

(94) Mrowetz, M.; Selli, E. Enhanced Photocatalytic Formation of Hydroxyl Radicals on Fluorinated TiO2. *Phys. Chem. Chem. Phys.* **2005**, *7*, 1100–1102.

(95) Moser, J.; Punchihewa, S.; Infelta, P. P.; Grätzel, M. Surface Complexation of Colloidal Semiconductors Strongly Enhances Interfacial Electron-Transfer Rates. *Langmuir* **1991**, *7*, 3012–3018.

(96) Wang, C. M.; Heller, A.; Gerischer, H. Palladium Catalysis of O2 Reduction by Electrons Accumulated on TiO2 Particles during Photoassisted Oxidation of Organic Compounds. *J. Am. Chem. Soc.* **1992**, *114*, 5230–5234.

(97) Gerischer, H.; Heller, A. The Role of Oxygen in Photooxidation of Organic Molecules on Semiconductor Particles. *J. Phys. Chem.* **1991**, *95*, 5261–5267.

TOC Graphic

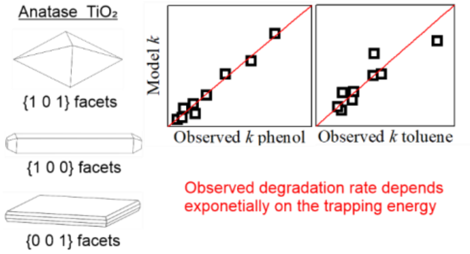

Observed degradation rate depends exponetially on the trapping energy